HHS Public Access

Author manuscript

Cell. Author manuscript; available in PMC 2021 August 06.

Published in final edited form as:

Cell. 2020 August 06; 182(3): 578–593.e19. doi:10.1016/j.cell.2020.06.031.

Cell types promoting goosebumps form a niche to regulate hair follicle stem cells

Yulia Shwartz[1,2,12], **Meryem Gonzalez-Celeiro**[1,2,3,12], **Chih-Lung Chen**[4,12], **H. Amalia Pasolli**[5], **Shu-Hsien Sheu**[6], **Sabrina Mai-Yi Fan**[4], **Farnaz Shamsi**[7], **Steven Assaad**[1,2], **Edrick Tai-Yu Lin**[4], **Bing Zhang**[1,2], **Pai-Chi Tsai**[1,2], **Megan He**[1,2,11], **Yu-Hua Tseng**[2,7], **Sung-Jan Lin**[4,8,9,10,*], **Ya-Chieh Hsu**[1,2,*]

[1]Department of Stem Cell and Regenerative Biology, Harvard University, MA 02138, USA. [2]Harvard Stem Cell Institute, Harvard University, Cambridge, MA 02138, USA. [3]Institute of Molecular Health Sciences, ETH Zurich, 8093 Zurich, Switzerland. [4]Department of Biomedical Engineering, College of Medicine and College of Engineering, National Taiwan University, Taipei 100, Taiwan. [5]Electron Microscopy Resource Center, The Rockefeller University, New York, NY 10065 [6]Janelia Research Campus, Howard Hughes Medical Institute, Ashburn, VA 20147. [7]Section on Integrative Physiology and Metabolism, Joslin Diabetes Center, Harvard Medical School, Boston, MA 02215, USA. [8]Department of Dermatology, National Taiwan University Hospital and National Taiwan University College of Medicine, Taipei 100, Taiwan. [9]Research Center for Developmental Biology and Regenerative Medicine, National Taiwan University, Taipei 100, Taiwan. [10]Graduate Institute of Clinical Medicine, College of Medicine, National Taiwan University, Taipei 100, Taiwan. [11]Department of Molecular and Cellular Biology, Harvard University, Cambridge, MA 02138, USA [12]Equal contribution

SUMMARY

Piloerection (goosebumps) requires concerted actions of the hair follicle, the arrector pili muscle (APM), and the sympathetic nerve, providing a model to study interactions across epithelium, mesenchyme, and nerves. Here, we show that APMs and sympathetic nerves form a dual component niche to modulate hair follicle stem cell (HFSC) activity. Sympathetic nerves form synapse-like structures with HFSCs and regulate HFSCs through norepinephrine, whereas APMs maintain sympathetic innervation to HFSCs. Without norepinephrine signaling, HFSCs enter deep quiescence by down-regulating cell cycle and metabolism while up-regulating quiescence regulators *Foxp1* and *Fgf18*. During development, HFSC progeny secretes Sonic Hedgehog (SHH)

*Correspondence to: Ya-Chieh Hsu, PhD (Lead Contact) yachieh_hsu@harvard.edu and Sung-Jan Lin, MD, PhD drsjlin@ntu.edu.tw.

AUTHOR CONTRIBUTION

Designing experiments: Y.S., M.G.C., C-L.C., Y-C.H, S-J.L. Conducted experiments: Y.S., M.G.C., C-L.C., S.M-Y.F., P-C.T., B.Z., F.S., S.A., E.T-Y.L., M.H. Intellectual contributions: Y-C.H., S-J.L., M.G.C., Y.S., C-L.C., H.A.P., S-H.S., Y-H.T. Writing the manuscript: Y-C. H, Y.S., M.G.C., S-J.L. with inputs from all authors.

DECLARATION OF INTEREST

Harvard intends to file a patent application based on the work.

to direct the formation of this APM-sympathetic nerve niche, which in turn controls hair follicle regeneration in adults. Our results reveal a reciprocal interdependence between a regenerative tissue and its niche at different stages and demonstrate sympathetic nerves can modulate stem cells through synapses-like connections and neurotransmitters to couple tissue production with demands.

eTOC/In Brief

The arrector pili muscle and the sympathetic neuron form a dual component niche that regulates hair follicle stem cells— the sympathetic neuron regulates stem cells directly with norepinephrine via synapse-like structures, while the arrector pili muscle maintains sympathetic innervation to stem cells. Through these three connected cell types, cold stimulates not only goosebumps but also stem cell activation.

Graphical abstract

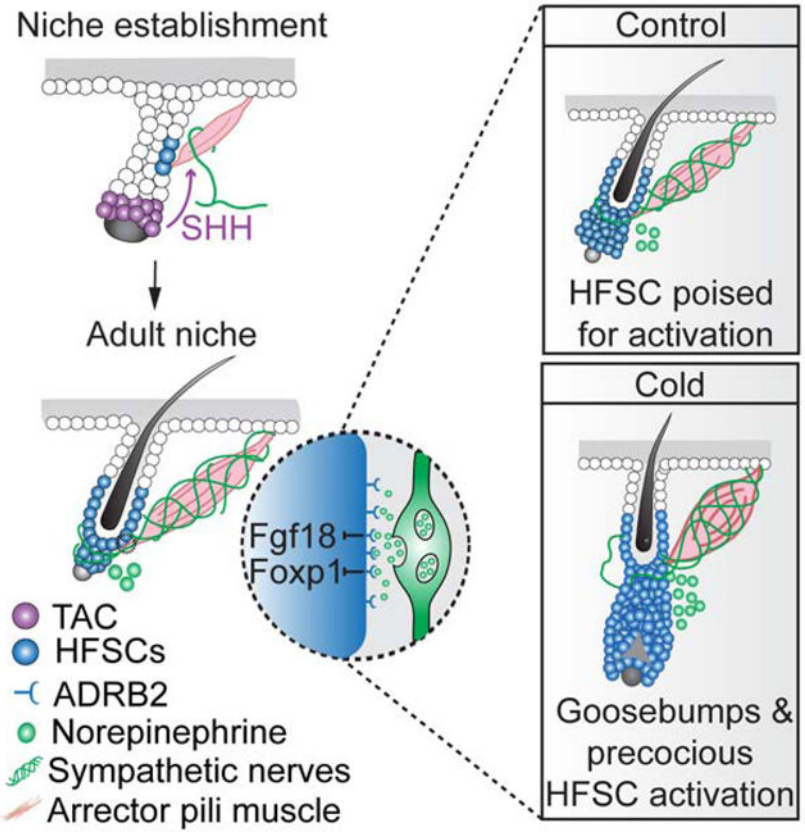

INTRODUCTION

Cell types from multiple lineages assemble into specific arrangements in organs. The functions of these cell types must be integrated to enable optimal outcomes in tissue homeostasis, maintenance, and function in an ever-changing environment, although the mechanisms of such integration are not well understood. Epithelium, mesenchyme, and

nerves are principle components of all organs. The sympathetic nervous system is a branch of the autonomic nervous system critical for maintaining body physiology under steady state and mediating “fightor-flight” responses following external insults. The cell bodies of sympathetic neurons reside in the sympathetic ganglia close to the spinal cord, while the axons extend out and innervate essentially all organs (Borden et al., 2013; Karemaker, 2017; Suo et al., 2015). Under steady state, the sympathetic neurons are active within a basal range to maintain diverse processes including heart rate, respiration and blood pressure. External stimuli, such as cold or danger, elevate the sympathetic nerve activity to different degrees according to the strength of the insult, allowing rapid changes in body physiology that enable animals to respond.

In the skin, the sympathetic innervation together with the arrector pili muscle (APM, mesenchymal origin) and the hair follicle (epithelial origin) form a tri-lineage unit (Figure S1A). The sympathetic nerve innervates APMs, which are bundles of smooth muscle cells (Furlan et al., 2016). APMs are attached to the bulge region of the hair follicle where hair follicle stem cells (HFSCs) reside (Fujiwara et al., 2011). Environmental stimuli, such as cold temperatures, have a pronounced effect on the tri-lineage unit: elevated impulses from sympathetic nerves trigger the contraction of APM bundles, pulling the hair erect, a phenomenon known as piloerection or goosebumps. The erected hair traps air to create a layer of insulation for thermoregulation. Besides piloerection, it is unclear whether there are other functions of this tri-lineage unit. Yet, this tri-lineage configuration is highly conserved across mammals including in humans, where piloerection has lost its role in thermoregulation, raising the possibility of additional functions.

Insight into such additional functions comes from the observation that changes in hair growth and changes in the sympathetic nervous system are often linked. The hair follicle undergoes rounds of rest (telogen) and growth (anagen), known as the hair cycle (Muller-Rover et al., 2001). HFSCs in the bulge and hair germ remain quiescent throughout most hair cycles, but become proliferative transiently at anagen onset to produce their transit-amplifying progeny — the matrix, which then undergoes massive proliferation and differentiation to fuel the growth of new hair (Greco et al., 2009; Hsu et al., 2014b; Lay et al., 2016; Rompolas et al., 2013; Wang et al., 2016; Zhang and Hsu, 2017; Zhang et al., 2009). It is known that loss of sympathetic innervation is associated with defects in hair growth in diverse organisms (Asada-Kubota, 1995; Botchkarev et al., 1999; Crowe et al., 1993; Kobayasi et al., 1958; Kong et al., 2015; Peters et al., 1999). In addition, adrenergic agonists promote anagen hair follicle growth in cultured skin explants, and external light stimulates hair growth via the sympathetic nervous system (Botchkarev et al., 1999; Fan et al., 2018).

These findings raise several key questions. First, given the broad impact of the sympathetic nervous system on whole body physiology and the diverse cell types that influence hair growth at the level of stem cell or niche, what are the direct cellular targets of the sympathetic neurons in hair growth control? Second, what are the cellular and molecular mechanisms by which sympathetic nerves regulate hair growth? Third, given that APMs are part of this tri-lineage unit, is there a role for APMs in regulating hair growth?

Here, we address these questions by combining cell-type specific gene deletion, cell ablation, transcriptome profiling, high-resolution imaging, and three-dimensional electron microscopy (3D-EM). We show that APMs are crucial for the formation and maintenance of sympathetic innervation to HFSCs, which allows sympathetic innervation to activate HFSCs directly through synapse-like connections that deliver the neurotransmitter norepinephrine. Under steady state, this nerve-APM-HFSC connection primes HFSCs for activation by lowering the expression of quiescence regulators *Foxp1* and *Fgf18*. Under cold conditions, the sympathetic nervous system is elevated, triggering not only goosebumps but also accelerating HFSC activation to produce new hair coat, coupling tissue growth with environmental changes. During development, the developing hair follicle initiates the formation of this tri-lineage unit through Sonic Hedgehog (SHH). Together, our findings illustrate an example of how cell types from the epithelium, mesenchyme, and nerve are integrated to allow tissue maintenance and function during development, homeostasis, and in response to environmental stimuli.

RESULTS

Sympathetic nerve activity regulates HFSC activity

The sympathetic nervous system is constantly active at a basal level to maintain body physiology. To explore if basal sympathetic nerve activity affects the other two cell types in this nerve-APM-HFSC tri-lineage unit, we ablated the sympathetic nerve in telogen skin through intradermal injection of 6-hydroxydopamine (6-OHDA, a selective neurotoxin for sympathetic nerves) (Kostrzewa and Jacobowitz, 1974), when HFSCs are quiescent. 6-OHDA ablated the sympathetic nerve efficiently, but spared the sensory nerves and other cell types in the skin (Figures 1A and S1B-S1E). Sympathectomy did not cause noticeable changes in APMs, but led to a substantial delay in HFSC activation and anagen entry (Figures 1B and S1E). By P30, hair follicles reached full anagen throughout the control back skin, whereas hair follicles in the sympathectomized skin remained mostly in telogen (Figure 1C). Similar results were obtained with a genetic model of sympathectomy by topical application of 4-OH-tamoxifen on *TH-CreER; Rosa-lsl-attenuated Diphtheria toxin fragment A (DTA)* mice (Figures 1D, S1F, and S1G). These results suggest that basal sympathetic nerve activity is required for HFSC activation and anagen entry but dispensable for APM maintenance.

Next, we explored the impact of elevated sympathetic tone on HFSC activation. Sympathetic nerve terminals secrete the neurotransmitter norepinephrine, which binds to adrenergic receptors on target cells. To elevate the sympathetic tone, we topically applied isoproterenol, a pan-adrenergic receptor agonist, at the extended 2nd telogen. Mice with topical application of isoproterenol entered anagen earlier (Figure 1E). Collectively, these data suggest that HFSC activity is tightly linked with sympathetic nerve activity. Loss of sympathetic nerve innervations makes HFSCs more dormant, whereas elevated sympathetic tone promotes HFSC activation.

The sympathetic nerve regulates HFSCs directly through norepinephrine-Adrb2 signaling

We then aimed to test if the sympathetic nerve regulates HFSCs directly. Sympathectomy led to diminished norepinephrine levels in the skin, suggesting that the sympathetic nerve is indeed a key source of norepinephrine in the skin (Figure S2A). By surveying RNA-sequencing (RNAseq) and ChIP-seq datasets (Ge et al., 2017; Lay et al., 2016; Lien et al., 2011), we found that *Adrb2* is the predominant adrenergic receptor expressed in HFSCs (Figures 2A, 2B, and S2B). To test if norepinephrine acts directly on HFSCs, we generated *K15-CrePGR; Adrb2 fl/fl* mice, in which *Adrb2* is depleted only from HFSCs (Figure 2C). *Adrb2*-cKO mice displayed significantly extended telogen length similar to the sympathectomized mice, suggesting that *Adrb2*-cKO HFSCs are refractory to activation (Figures 2D and S2C). Other than the delayed anagen entry, *Adrb2*-cKO mice showed no changes in sympathetic innervation and no signs of abnormal cell death (Figures S2D and S2E). Moreover, topical application of an ADRB2-specific agonist (procaterol) at the extended 2nd telogen accelerated anagen entry (Figure 2E). These data suggest that loss of ADRB2 inhibits HFSC activation, whereas elevation of ADRB2 activity promotes HFSC activation. Moreover, addition of procaterol onto cultured human HFSCs promoted their growth, suggesting the pathway has a conserved function in regulating human HFSCs (Figure 2F).

ADRB2 binds to both norepinephrine and epinephrine. In addition to the sympathetic nerve, adrenal glands secrete epinephrine and norepinephrine (collectively known as catecholamines) into the bloodstream. To test if adrenal gland-derived catecholamines regulate HFSCs, we removed both adrenal glands and supplied back corticosterone, another adrenal gland-derived hormone (Figures S2F-S2I). Unlike sympathectomized mice, adrenalectomized mice supplemented with corticosterone had no delays in anagen entry (Figure S2J), suggesting that adrenal gland-derived catecholamines are dispensable for HFSC activation. These data establish that the sympathetic nerve secretes norepinephrine, which binds to ADRB2 on HFSCs to modulate stem cell activity directly.

Transcriptomic analyses of *Adrb2*-deficient HFSCs

To identify the molecular underpinnings of the delay in hair cycle entry when HFSCs lack *Adrb2*, we conducted RNA-seq analysis of FACS-purified HFSCs. To pinpoint the functional differences that drive changes, we deleted *Adrb2* in telogen and isolated HFSCs when both the control and *Adrb2*-depleted hair follicles were still in telogen, as confirmed by histological analyses (Figures 3A, 3B, and S3A). Principal component analysis showed that replicates clustered according to genotypes (Figures 3C and S3B). RNA-seq confirmed that *Adrb2* is efficiently depleted in HFSCs (Figure S3C). Ingenuity pathway analysis (IPA) and Gene Ontology (GO) enrichment analysis revealed that cell cycle related categories (including cell division machinery, cell cycle control, and cell cycle checkpoint) were featured as some of the most significantly downregulated changes in *Adrb2*-depleted HFSCs (Figures 3D and 3E and S3D). These results suggest that even at telogen, *Adrb2*-depleted HFSCs have already down-regulated cell cycle machinery. Moreover, genes related to oxidative phosphorylation, mitochondria function, and ribosomal components were also down-regulated (Figures S3D-S3F). Similar categories were featured as hallmarks that distinguish quiescent neural stem cells and muscle stem cells that are more dormant from

those that are primed for activation (Llorens-Bobadilla et al., 2015; Rodgers et al., 2014; van Velthoven et al., 2017).

Our transcriptomic data also showed several genes known to regulate HFSC quiescence become up-regulated in HFSCs upon *Adrb2* depletion (Figure 3F), including the transcription factor *Foxp1* and its downstream target *Fgf18* (Hsu et al., 2011; Kimura-Ueki et al., 2012; Leishman et al., 2013) (Figure 3G). The up-regulation of *Fgf18* in *Adrb2*-depleted HFSCs is particularly notable. HFSCs are located in the outer bulge layer that is innervated by the sympathetic nerve, adjacent to an inner K6+ differentiated bulge layer that is not innervated (Figure 3H, see also innervation analyses below). In wild-type mice, *Fgf18* is highly expressed in the inner K6+ bulge but lower in HFSCs (Hsu et al., 2011). By contrast, in *Adrb2*-cKO mice, *Fgf18* becomes up-regulated in HFSCs as well, as verified by *in situ* hybridization (Figure 3I). These data suggest that sympathetic innervation keeps *Fgf18* levels low at the outer bulge layer where HFSCs reside (Figures 3I and S3G). Moreover, overexpression of *Fgf18* through injection of Adeno-Associated Viruses (AAVs) (Goldstein et al., 2019) expressing *Fgf18* under the control of a CAG promoter suppressed anagen entry (Figures 3J and S3H). Together, our data show that upon *Adrb2* deletion, HFSCs enter a deep quiescent state governed in part by up-regulation of the *Foxp1-Fgf18* axis. These findings link a quiescence pathway with an upstream neuronal signal.

The sympathetic nerve wraps around HFSCs

The sensitivity of HFSCs to basal levels of sympathetic nerve activity is notable given that the sympathetic nerve regulates other stem cells either indirectly via the niche or only upon hyperactivation (Katayama et al., 2006; Lucas et al., 2013; Maryanovich et al., 2018; Zhang et al., 2020). We therefore sought to elucidate the cellular basis of the sympathetic nerve-HFSC interaction that might account for the sensitivity of HFSCs to low levels of norepinephrine. 3-D reconstructed images of thick skin sections (100 μm) revealed that sympathetic nerves form an elaborate neuronal network in the skin (Figures 4A and S4A). Consistent with previous findings, we found that each APM intermingled with dense sympathetic nerve bundles, forming the cellular basis of piloerection (Botchkarev et al., 1999; Furlan et al., 2016) (Figure 4B and Video S1). Interestingly, many sympathetic nerve fibers extended beyond the APMs and approached the HFSCs located at different positions throughout the outer bulge and the hair germ (Figures 4B, 4C, S4B, S4C, and Video S1). The interaction between sympathetic nerves and HFSCs was not restricted to the sites where APMs attach to the hair follicle (the caudal side). In the 2nd telogen when a new bulge and hair germ form at the rostral side of the APMs, we observed sympathetic fibers innervating both the old and new bulge (Figures 4C, S4C, and Video S2). HFSCs were often innervated by sympathetic nerve fibers that branch out from the dense sympathetic bundles along APMs (Figures 4C and S4C left). In some cases, sympathetic nerves approached the new bulge and hair germ from the rostral side, branching from connected bridges linking each sympathetic nerve bundle (Figures 4C and S4C right). 3Dreconstructed images confirmed that sympathetic innervations wrap around both the old and new bulge (Figures 4C', S4C', and Video S2). Orthogonal sections showed that sympathetic nerves form multiple contact points with HFSCs located at the old bulge, new bulge, or hair germ (Figures 4C", S4C", and

Video S2). Collectively, these data suggest that sympathetic nerves innervate not just the APMs but also the HFSCs located throughout the outer bulge and hair germ.

Sympathetic nerves form synapse-like connections with HFSCs

Sympathetic nerves innervate smooth muscles or glands to exert their functions through synapses (also known as neuroeffector junctions), allowing efficient activation of intended targets. Epithelial cells like HFSCs are not conventional synaptic targets, but the proximity between nerve endings and HFSCs and the sensitivity of HFSCs to low levels of norepinephrine, prompted us to examine if sympathetic nerves might form synapse-like connections with HFSCs. Immunofluorescent staining showed that sympathetic nerve fibers colocalize with the pre-synaptic markers synaptotagmin and synaptophysin, (Figures 4D and S4D), as well as VMAT2 (Vesicular monoamine transporter 2, marking norepinephrinecontaining synaptic vesicles, Figure S4E), when approaching HFSCs, suggesting that these are terminal axons with norepinephrine vesicles reaching their targets. Furthermore, when sympathetic axons approached HFSCs, we identified swellings of the axon that resemble axonal varicosities (or boutons), structures at the synaptic terminals where neurotransmitters are stored (Figure 4E). To examine the interactions between nerves and HFSCs, we conducted serial block face scanning EM (Swanson and Lichtman, 2016). 3D-EM reconstructions confirmed the presence of axonal varicosities around HFSCs (Figure 4F). EM data showed that the sympathetic fibers were wrapped by Schwann cells. These wrapped nerve fibers were then bundled and enclosed by the endoneurium composed of specialized fibroblasts and collagen. As the sympathetic nerve bundle approached HFSCs, the endoneurium opened only on the side that faces HFSCs, exposing nerve fibers to HFSCs (Figures 4G and S4F). This opening likely facilitates the diffusion of neurotransmitters toward HFSCs, as the endoneurium may blunt their transmission. We also observed exposed axons without Schwann cell wrappings at the side where the sympathetic fibers face HFSCs, which may further enhance the transmission of neurotransmitters to HFSCs (Figures 4F, S4G, and S4H). Moreover, we observed vesicles and mitochondria (crucial for synaptic transmissions) when these exposed axons approach HFSCs (Figures 4F and S4H). These features are morphologically distinct from sensory nerves, which are encased by terminal Schwann cells (Li and Ginty, 2014) (Figure S4I). These cellular characteristics suggest that sympathetic nerves form synapse-like connections with HFSCs, reminiscent of those found in autonomic neuromuscular junctions or parasympathetic innervation at salivary glands (Burnstock, 2008; Sheu et al., 2017).

The sympathetic nerve-HFSC interaction is maintained by APMs

We next explored how these nerve-stem cell interactions are maintained in the skin, where dynamic changes occur in both the epithelium and mesenchyme. We first tested if HFSCs are responsible for maintaining these nerve-stem cell interactions. However, upon HFSC ablation, we could still detect sympathetic innervation towards HFSCs, suggesting that HFSCs are not essential in maintaining these nerve-HFSC interactions (Figure S5A).

Given that sympathetic nerve fibers were intertwined with APMs, we next sought to determine if APMs are essential for maintaining sympathetic innervation to HFSCs. To this end, we generated a transgenic mouse model in which both the YFP reporter and the

diphtheria toxin receptor (DTR) are expressed under the smooth muscle actin (SMA) promoter (*SMA-YFP-DTR* mouse, Figure 5A). YFP staining confirmed that the SMA promoter was active in the APMs but not the dermal sheath in telogen (Figure 5B, left panel). When we injected diphtheria toxin (DT) intradermally to the *SMA-YFP-DTR* mice in telogen, active Caspase-3 staining was prominent in APMs, indicating APMs were effectively ablated (Figure S5B). By contrast, other cell types including dermal papilla, dermal sheath, capillaries surrounding HFSCs, and smooth muscle cells in the subcutaneous vessels remained largely unaffected (Figures 5B, and S5C-S5E). These data confirm that our *SMA-YFP-DTR* mouse coupled with intradermal DT injection preferentially ablates APMs. When we examined sympathetic innervation in these APM-ablated mice, we found that the sympathetic innervation to HFSCs was lost concomitantly following APM ablation (Figures 5C and 5D). Collectively, these data show that APMs are essential for maintaining the sympathetic innervation to HFSCs. Similar to sympathectomized mice, these APM-ablated mice also displayed a delay in anagen entry (Figure 5E).

To further confirm the role of APMs in maintaining sympathetic innervation to HFSCs, we established another method to specifically ablate APMs. Intradermal injection of AAV-PHP.S infected APMs and some fibroblasts, but not blood vessels, dermal sheath, sympathetic nerves, or smooth muscles in the subcutaneous vessels (Figures S5F-S5J). Intradermal injection of a Cre inducible DTA construct (Wu et al., 2014) supplied by AAV-PHP.S into *Myh11-CreER* mice allowed us to achieve specific APM ablation, as APMs are the only cells in the body that carry both CreER and flex-DTA (Figure 5F). Consistent with the *SMA-YFP-DTR* model, ablation of APMs leads to loss of sympathetic innervation to HFSCs in *Myh11-CreER; AAV-flex-DTA* mice (Figure 5F). Together, these data establish a crucial role of APMs in maintaining the sympathetic innervation to HFSCs.

Many epidermal and dermal cell types in the skin undergo substantial turnover (Driskell et al., 2013; Heitman et al., 2020; Hsu et al., 2014a; Rivera-Gonzalez et al., 2016; Rompolas et al., 2016; Sada et al., 2016; Zhang et al., 2016), which poses challenges to the maintenance of constant innervation. To determine if APMs also undergo turnover, we conducted lineage-tracing experiments. We labeled APMs at the 1st telogen in *Myh11-CreER; Rosa-lsl-YFP* mice. Three days after tamoxifen treatment, the majority of the APM fibers became YFP positive (Figure 5G). The percentage of labeled APMs did not change over several rounds of hair cycles over a 5-month period. Without tamoxifen, the Myh11-CreER showed minimal leakiness (Figure S5K). These data suggest that APMs do not undergo major turnover. In this sense, APMs serve as a critical structural support to which sympathetic nerves can remain anchored while both the epithelial and mesenchymal compartments undergo periodical remodeling.

Cold triggers both piloerection and hair growth

Our data established that APMs and sympathetic innervation form a dual component niche to regulate HFSC activity. The sympathetic nerve secretes norepinephrine to modulate HFSC activity directly, while APMs maintain sympathetic nerve-HFSC interactions. One known process that requires the concerted action of this tri-lineage unit is piloerection.

Given our findings, we predicted that the elevated sympathetic nerve activity in response to cold may not only induce goosebumps, but might also promote HFSC activation.

To explore this idea, we compared sex-matched, age-matched telogen mice under cold vs. thermoneutral conditions. Cold exposure indeed enhanced sympathetic nerve activity, as evidenced by elevated c-FOS expression in the sympathetic ganglia (where cell bodies of sympathetic neurons reside) of mice exposed to cold (Figures 6A and 6B). In agreement with this, the level of norepinephrine was also up-regulated in the skin upon cold stimulation (Figure 6C). Mice displayed the classical goosebumps reaction in response to cold (Figure 6D). Moreover, mice exposed to cold entered anagen precociously to produce new hairs within less than 2 weeks (Figures 6E and 6F). These data demonstrate that temperature changes trigger two reactions — erection of hairs to trap air for thermoregulation and acceleration of HFSC activation to promote the production of a new hair coat.

SHH secreted from the developing hair follicles regulates APM formation and sympathetic innervation

Having established the interconnectivity and function of this tri-lineage unit in tissue regeneration in adults, we next explored how this APM-sympathetic nerve niche is established developmentally. We first determined the developmental timing of APMs and sympathetic innervation to HFSCs. Hair follicles develop in three waves (Andl et al., 2002; Schmidt-Ullrich and Paus, 2005). By postnatal day P1, APMs appeared around the down-growing hair follicles formed during the 1st wave but were absent from the budding hair follicles that just emerged at the 3rd wave. By P2, we found APMs in all hair follicles as they matured. By contrast, sympathetic nerves only began to innervate APMs around P5. By P8, the sympathetic innervation to both APMs and HFSCs became apparent (Figures 7A and 7B). These results demonstrate the hair follicle is the first tissue to form in this tri-lineage unit, followed by APM, and the sympathetic nerve only innervates HFSCs after APMs form and mature.

Given that the emergence of APMs correlates with the degree of maturation in the hair follicle, we explored if signals from the hair follicle regulate APM formation. One candidate signal is SHH, a long-range secreted protein from transit-amplifying cells of the developing hair follicle (HF-TACs) (St-Jacques et al., 1998; Zhang and Hsu, 2017). Through SHH, HF-TACs regulate diverse processes including hair follicle downgrowth, dermal adipocyte production, and Merkel cell formation (Chiang et al., 1999; Hsu et al., 2014b; Perdigoto et al., 2016; Woo et al., 2012; Xiao et al., 2016; Zhang et al., 2016). We found developing APMs were positive for *Gli1*, a target of Hedgehog (HH) signaling (Figure 7C).

To determine if HH signaling regulates APM formation, we deleted *Smoothened* (*Smo,* a component required for HH signal transmission) from the dermis using *Pdgfra-Cre*. Lineage analysis confirmed that APMs but not sympathetic neurons are derived from PDGFRA positive dermal fibroblasts (Driskell et al., 2013) (Figure S6A and S6B). *Pdgfra-Cre*; *Smo fl/fl* mice could form HFSCs and differentiated progeny, but lacked APMs, suggesting that HH signaling is required for APM formation (Figures 7D and S6C-S6G).

We then asked if sympathetic innervation to the developing HFSCs requires APMs. *Pdgfra-Cre*; *Smo fl/fl* mice not only lacked APMs but also lacked sympathetic innervation to HFSCs (Figure 7E), suggesting that APMs establish the sympathetic innervation to HFSCs during development. This lack of sympathetic innervation was unlikely due to a requirement of *Smo* in the sympathetic nerve itself, because *Pdgfra-Cre* was not expressed in sympathetic neurons (Figure S6B). Collectively, these data suggest that HH signaling regulates the formation of APMs. Once APMs form, they then attract sympathetic innervation to HFSCs.

Next, we aimed to identify the source of HH that regulates APM formation. *Ihh* is not expressed in the skin (Rezza et al., 2016; Sennett et al., 2015) (Figure S7A), and *Dhh* mutants still developed APMs (Figure S7B). However, when *Shh* was depleted from developing hair follicles by K14-Cre, APMs failed to form (Figure 7F). By contrast, APMs remained intact when *Shh* was depleted from the sensory nerves (Figure S7C), another source of SHH in the skin (Brownell et al., 2011; Zurborg et al., 2011). These data suggest that SHH from the developing hair follicle drives APM development.

SHH regulates hair follicle downgrowth (Chiang et al., 1999; St-Jacques et al., 1998; Woo et al., 2012). As such, the hair follicle in the *K14-Cre; Shh fl/fl* skin is defective. To determine if lack of APMs was due to defects in hair follicle growth in the *K14-Cre; Shh fl/fl* skin, we established a *K14-Cre; Rosa-lsl-rtTA; TetO-P27* model to block the downgrowth of hair follicles without affecting *Shh* expression (Figures 7G, 7H, S7D, and S7E). APMs were present in *K14-Cre; Rosa-lsl-rtTA; TetO-P27* skin, despite severe defects in hair follicle downgrowth and development (Figures 7G and S7E). These data suggest that defects in hair follicle development do not cause APM loss as long as *Shh* is present. APMs attach to the bulge via the integrin Nephronectin, but APMs still form in *Nephronectin* mutants (Fujiwara et al., 2011). Nephronectin expression also remained intact in both *K14-Cre; Shh fl/fl* and *Pdgfra-Cre; Smo fl/fl* skins, suggesting that mechanisms regulating APM formation and APM attachment are distinct (Figures 7I and 7J). In conclusion, our data demonstrate a reciprocal interaction between the hair follicle and its APM-sympathetic nerve niche at different stages. During development, hair follicles control the formation of APMs that then attract sympathetic innervations. In adults, sympathetic innervations, anchored on APMs, activate HFSCs and promote hair follicle regeneration (Figure S7F).

DISCUSSION

Cell types enabling goosebumps form a dual component niche for HFSCs

The erection of hairs, feathers, and spines plays a role in thermoregulation, courtship, and aggression, features essential for evolutionary success across the animal kingdom (Darwin, 1872). The anatomical connection between APMs and HFSCs is conserved across mammals, raising the possibility that there might be evolutionary advantages to preserving this anatomical connection beyond goosebumps. We find that cell types enabling goosebumps form a dual component niche for HFSCs: a supporting component (the APM) and a signaling component (the sympathetic nerve), with the former maintaining the latter. It is possible the APM is evolutionarily conserved due to its indispensable role as a hub to attract and maintain sympathetic innervations in the skin.

Sympathetic neurons differ from other niche cell types for HFSCs (Chen et al., 2020) in that they are both a niche component and a systemic regulator. As a part of the autonomic nervous system, sympathetic innervation provides a direct channel to rapidly transmit systemic changes into local tissue changes. This direct system-to-local connection may allow the activation threshold of HFSCs to vary in response to temperature, circadian rhythm, or physiological changes. In this sense, goosebumps may only be the first line of defense in responding to cold. When cold conditions persist, elevated sympathetic nerve activity allows HFSCs to exit quiescence and initiate hair follicle regeneration to make new hair, coupling stem cell activity and tissue production with outside environmental changes (Figure S7G).

APMs are often lost in the scalp skin of people with androgenetic alopecia (common baldness) (Torkamani et al., 2014; Yazdabadi et al., 2012). It is possible that in such skin, loss of APMs leads to the loss of sympathetic nerves, making HFSCs more difficult to activate. Our results also suggest the potential of using selective β2 agonists to promote HFSC activation.

The impact of sympathetic nerve activity on different stem cell populations

The sympathetic nerve is known to influence melanocyte stem cells (MeSCs), a distinct stem cell population also located around the bulge that regenerates the pigment to color the hair (Zhang et al., 2020). Hyperactivation of sympathetic neurons, as occurs in severe stress, depletes MeSCs, forming the basis for stress-induced hair graying. There are several interesting differences regarding how the sympathetic nerve regulates MeSCs vs. HFSCs. First, HFSCs are more sensitive to low levels of sympathetic nerve activity than MeSCs. HFSCs respond to both basal and modest elevation of sympathetic tone (such as in cold), a characteristic likely facilitated by the synapse-like connections between sympathetic nerve terminals and HFSCs. By contrast, MeSCs are only depleted upon sympathetic nerve hyper-activation. MeSCs are outside of the synaptic transmission range (~1–2 μm for sympathetic nerve), and are likely influenced by norepinephrine mostly through diffusion, which is only effective at high concentrations. Moreover, whereas HFSCs are positively regulated by the sympathetic nerve to produce tissues, MeSCs are negatively affected. It is likely that the sympathetic nerve innervates the hair follicle to regulate HFSCs, while depletion of MeSCs is an undesired side effect when the nerve activity is abnormally high. Future studies are needed to explore how the sympathetic nerve drives different outcomes for distinct stem cells based on differences in the amplitude and duration of nerve activation.

There are also interesting similarities and parallels between the skin and the bone marrow. In both systems, there is a close interplay among stem cells, nerves, and mesenchyme. In the skin, sympathetic nerves regulate HFSCs directly through innervation, and the mesenchymal component (APMs) maintain this nerve-stem cell interaction. In the bone marrow, sympathetic nerves regulate hematopoietic stem cell retention and egression indirectly by regulating *Cxcl12* expression in the mesenchyme (Heidt et al., 2014; Katayama et al., 2006).

Epithelial stem cells are an unconventional post-synaptic target

Neurons regulate excitable targets (e.g. neurons or muscles) through synapses. Here we show that sympathetic nerves can also modulate an epithelial stem cell, an unconventional target, through a classical neurotransmitter with synapse-like connections. Neurotransmitters are unstable, so synapse-like structures minimize random diffusion of neurotransmitters and direct them towards the intended targets. Here, the short-range effect of norepinephrine is further propagated by regulating a secreted protein FGF18 that is more stable and has a longer working distance. This allows the nerve signal to extend beyond HFSCs that are innervated to other HFSCs that may not receive direct innervation (Figure S3G). Such a relay mechanism may be widely applicable when considering how innervations and neurotransmitters can modulate a wide variety of biological processes outside of the nervous system with limited innervation sites.

Sympathetic nerve innervates smooth muscles, glands, and endocrine cells across the body. We postulate that some cell types adjacent to these conventional nerve targets may also receive direct neuronal input with similar structures and mechanisms as we describe here for HFSCs. In particular, epithelial stem cells (for example, those in the airway or gut), which are in close proximity to smooth muscle cells, are prime candidates for this type of regulation. It is also possible that cancer cells hijack similar mechanisms to connect with the nervous system, as solid tumors are often highly innervated (Kamiya et al., 2019; Peterson et al., 2015; Venkataramani et al., 2019; Venkatesh et al., 2019; Zahalka et al., 2017). Collectively, our findings reveal the cellular and molecular mechanisms underlying the interaction between the sympathetic nervous system and an unconventional target, opening up future avenues for investigation into the potentially broad function of such interactions.

STAR METHODS

RESOURCE AVAILABILITY

Lead Contact—Further information and requests for resources and reagents should be directed to and will be fulfilled by the Lead Contact, Ya-Chieh Hsu (yachieh_hsu@harvard.edu).

Materials Availability—All unique reagents generated in this study are available from the Lead Contact.

Data and Code Availability—The RNAseq data generated during this study are available at GEO accession code GSE130240

EXPERIMENTAL MODEL AND SUBJECT DETAILS

Mouse lines—*K15-CrePGR* (Morris et al., 2004), *K14-Cre* (Dassule et al., 2000), *Smo fl/fl* (Long et al., 2001), *Shh fl/fl* (Lewis et al., 2001), *Rosa-lsl-YFP* (Srinivas et al., 2001), *Pdgfra-Cre* (Roesch et al., 2008), *Advillin-Cre* (Zurborg et al., 2011), *Myh11-CreER* (Wirth et al., 2008), *Adrb2 fl/fl* (Hinoi et al., 2008), *Gli1-Lacz* (Bai et al., 2002), *Rosa-lsl-DTA* (Voehringer et al., 2008), *Rosa-lsl-attenuated DTA* (Wu et al., 2006), *Dhh* −/− (Bitgood et al., 1996), *Rosa-rtTA-IRES-EGFP (Rosa-lsl-rtTA)* (Belteki et al., 2005), *TetO-P27* (Pruitt et

al., 2013), and *TH-CreER* (Abraira et al., 2017) mice were described previously. The *SMA-YFP-DTR* transgenic mouse line was generated as follows. The plasmid pACTA2-YFP-P2A-DTR was constructed by replacing the CMV promoter region of pcDNA3.1 with the 4-kilobase (kb) fragment of the mouse ACTA2 promoter/intron derived from C57BL/6 genomic DNA. The human HB-EGF cDNA and YFP cDNA were ligated with P2A and cloned into a pcDNA3.1-ACTA2 plasmid. The 6.2-kb *MfeI/DraIII* fragment from pACTA2-YFP-P2A-DTR was microinjected as a transgene into fertilized mouse eggs (C57BL/6), which were then implanted into pseudo-pregnant female mice (C57BL/6). Integration of the transgene was checked by PCR analysis of DNA extracted from tail tissues. All procedures were performed with animal protocols approved by the Institutional Animal Care and Use Committee at Harvard University, Joslin Diabetes Center, or National Taiwan University. All mice used were specific-pathogen free and housed in individually ventilated cages (max. 5 per cage) under a 12:12 light-dark cycle at 21–25°C and 30%−75% humidity. Housing and husbandry conditions for cold exposure experiments are described as bellow. Mice were fed ad libitum with rodent diet (LabDiet Prolab Isopro RMH 3000 5P75 or PicoLab Mouse Diet 20 5058) and water. Animal health was monitored daily. Surveillance for infectious agents was performed quarterly. All procedures and treatments are described as in Method Details. None of the mice were involved in any previous procedures prior to the study.

METHOD DETAILS

Cold Exposure—Individually caged C57BL/6J mice (JAX 00064 sex- and age-matched) were housed at an ambient temperature of 5°C for a period of 2 hours or 2 weeks. Control animals were individually caged and housed at a thermoneutral (30°C) temperature. Both groups of mice were housed in a controlled environmental diurnal chamber (Caron Products & Services Inc., Marietta, OH) with free access to food and water.

***In Situ* Hybridization—**Unfixed dorsal skin samples (12 – 16 μm thick sections) were collected and embedded in OCT. *In situ* hybridization was performed using an ACD RNAScope kit (2.5 HD assay-Red) according to the manufacturer's protocol with the following modifications. For *Fgf18* (495421) *in situ*, the slides were incubated for 40 minutes with Protease III and incubated for 45 minutes with Amp5. For *Shh* (314361), *in situ* was performed according to the manufacturer's protocol.

Adrenalectomy—P19 C57BL/6J mice were anesthetized. Both adrenal glands were removed using curved forceps through 2 small incisions. Sex- and aged-matched controls underwent a sham operation using an identical procedure, except their adrenal glands were not removed. Adrenalectomized mice were given drinking water with 1% NaCl following surgery and were provided with corticosterone supplemented water from P21 onwards. Sham mice were provided with vehicle solution. Corticosterone water was prepared by dissolving 35 μg/ml corticosterone (Sigma 27840) in 0.66% (2-Hydroxypropyl)-β-cyclodextrin (Sigma 778966).

Hormone measurements—For corticosterone, norepinephrine, and epinephrine measurements following adrenalectomy and sham surgery, blood plasma was used. Following euthanasia, blood was collected from the heart, transferred to Microvette 300

Capillary Blood Collection Tubes (Fischer Scientific 22–043975), and centrifuged at 3000g for 2 minutes. Plasma was transferred to new tubes and stored at −80°C prior to hormone measurements. Hormone measurements were performed using the following ELISA kits, according to the manufacturers' protocols: Corticosterone ELISA kit (ARBOR ASSAYS, KO14-H1), Epinephrine ELISA kit (Abnova KA3837), and Norepinephrine ELISA kit (Abnova KA1891).

For norepinephrine measurements in the skin (following sympathectomy or cold exposure), a 4-mm punch biopsy was used to collect full thickness skin (approximately 25 mg). The skin was homogenized in 40 μl lysis buffer, and norepinephrine concentration was determined using a Norepinephrine ELISA kit (MYBioSource, MBS2600834) according to the manufacturer's protocol.

AAV generation and administration—The following constructs were used: pAAV-CAG-tdTomato (Addgene plasmid #59462) was used to generate AAV-PHP.S-CAG-tdTomato virus (Addgene); and pAAV-mCherry-flex-DTA (Addgene plasmid #58536) was used to generate AAV2/PHP.S-mCherry-flex-DTA virus (BCH viral core). For FGF18 overexpression, the coding sequence of *Fgf18* (with HA tag) was cloned into the pAAV backbone. The plasmid was further used to generate AAV8-CAG-FGF18–3XHA virus (Welgen).

All AAV viruses were injected intradermally. Viral stock was diluted to a concentration of 1E12 gc/ml with saline (0.9% NaCl). 50 μl of the diluted virus was injected once intradermally. Dorsal skin was collected 6 days following injection of AAV-PHP.S-CAG-tdTomato, 10 days following AAV8-CAG-FGF18–3XHA injection, and 18 days following AAV2/PHP.S-mCherry-flex-DTA. For APM ablation, AAV2/PHP.S-mCherry-flex-DTA was injected as described above into *Myh11-CreER* mice.

Doxycycline administration—Timed-pregnant females were administrated with 300 μl of Doxycycline (Sigma D3447 10 mg/ml) by oral gavage and switched to a Doxycycline rodent diet (S3888) from E15.5.

Topical tamoxifen treatment—A solution of 20 mg/ml Tamoxifen (Sigma T5648) in 100% ethanol was used for topical Tamoxifen treatment. The dorsal skin of *Myh11-CreER; Rosa-lsl-YFP* mice was shaved prior to treatment. Tamoxifen (100 μl) was applied topically once a day during first telogen at P20-P22. A solution of 10 mg/ml 4-Hydroxytamoxifen (Sigma H6278) in 100% ethanol was used for all 4-Hydroxytamoxifen topical treatments. The dorsal skin of *TH-CreER; Rosa-lsl-DTA* mice was shaved prior to treatment. 4-Hydroxytamoxifen (100 μl) was applied topically once a day at P20P24. For APM ablation, AAV2/PHP.S-mCherry-flex-DTA was injected as described above into *Myh11-CreER* mice. 4 days following injection, 4-Hydroxytamoxifen (200 μl) was applied topically once a day for 6 days. Control mice were treated with 100% ethanol.

Colony formation assay (CFA)—Human hair follicles were isolated from normal scalp tissues. To isolate hair follicle stem cells (HFSCs), hair follicles were dissected, and subcutaneous fat and connective tissues were carefully removed with a scalpel. The lower

hair bulb and upper epithelial layer were removed as previously described (Oshima et al., 2001; Rochat et al., 1994). For HFSC isolation, hair follicles were incubated in 1.25 U/mL dispase (Gibco) and 0.5 mg/mL collagenase I (Sigma-Aldrich) solution at 37°C for 30 minutes, following which the mesenchymal sheath was carefully removed with forceps. To obtain a single cell HFSC suspension, tissue was digested with 0.05% trypsin/EDTA solution (Gibco) for 1 h at 37°C, and cells were filtered through a sterile 40-μm cell strainer (BD Biosciences). Single cell suspensions were then centrifuged at 1300 rpm for 10 minutes and plated on mitomycin C (Cayman) treated J2 feeders at a cell density of 5000 cells/well in a 12-well culture plate (Falcon) in E media supplemented with EGF and additives as described in (Mou et al., 2016; Nowak and Fuchs, 2009). After 48 hours, 0.1 μM procaterol (Sigma) was added (freshly prepared). Medium was changed every 2 days. On day 10, plates were fixed with 4% PFA and stained with Rhodamine B (Sigma). All experiments involving human samples were approved by Institutional Review Board of National Taiwan University and informed consent was obtained from patients undergoing routine scalp skin surgery. CFA quantification was done using Fiji.

Sympathetic nerve ablation—Chemical ablation: 6-Hydroxydopamine hydrobromide (6-OHDA, Sigma 162957) solution was prepared freshly by dissolving 6-OHDA in 0.1% ascorbic acid (in 0.9% sterile NaCl) for intradermal injection. For intradermal injection, 0.6 mg of 6-OHDA was dissolved in 100 μl 0.1% ascorbic acid, and mice were injected at P18 or P19. Control animals were injected with vehicle (100 μl of 0.1% ascorbic acid). For norepinephrine measurements in the skin, following sympathetic nerve ablation, 7-week-old mice were used. 6-Hydroxydopamine hydrobromide (6-OHDA, Sigma 162957) solution was prepared freshly by dissolving 6-OHDA in 0.2% ascorbic acid (in 0.9% sterile NaCl). Mice were injected intraperitoneally for two consecutive days with the following doses: 250 mg/kg body weight and 100 mg/kg body weight. Skin was analyzed one week after ablation.

EdU administration—Two doses of EdU were administered by intraperitoneal injection before harvesting. The first injection was done 8 hours before harvesting, and the second one was done 4 hours before harvesting. 25 μg EdU/g body weight was injected each time (dissolved in 0.9% NaCl).

Histology and immunohistochemistry—Dorsal skin samples were fixed for 15 minutes using 4% paraformaldehyde (PFA) at room temperature, washed with PBS, immersed in 30% sucrose overnight at 4°C, and embedded in OCT (Sakura Finetek). 50-μm sections were used for all staining unless otherwise noted. For all 50-μm thick immunofluorescent staining, slides were blocked (5% Donkey serum, 1% BSA, 2% Cold water fish gelatin, and 0.3% Triton in PBS) for 1 – 4 hours at room temperature, incubated with primary antibody overnight at 4°C, then incubated with secondary antibody for 2 – 4 hours at room temperature or overnight at 4°C. For Figures 4A–4C, S4A, S4B, and 5D, 100-μm thick sections were used. Slides were blocked (5% Donkey serum, 1% BSA, 2% Cold water fish gelatin, and 0.3% Triton in PBS) for 1 – 4 hours at room temperature, incubated with primary antibody for 48 hours at 4°C, then incubated with secondary antibody for 48 hours at 4°C. For Figures S5B and S5C, dorsal skin was fixed in 4% PFA at 4°C overnight. Samples were washed with PBS and embedded in OCT for 100-μm thick sectioning.

Sections were blocked (PBS, 5% BSA, 1% Tween20) for 12 hours at 4°C, incubated with primary antibodies for 2 days at 4°C, then incubated with secondary antibodies for 2 days at 4°C. The following antibodies and dilutions were used: CD34 (rat, eBioscience 14–0341-85, 1:100); phospho-histone H3 (rabbit, Cell Signaling Technology 3377S, 1:250); cleaved Caspase 3 (rabbit, Cell Signaling Technology 9664S, 1:100 – 1:300); PCAD (goat, R&D AF761, 1:400); Tyrosine hydroxylase (rabbit, Millipore AB152, 1:1000; sheep, Millipore AB1542, 1:150 – 1:300 or chicken, Millipore AB9720, 1:50); GFP (rabbit, Abcam ab290, 1:5000 or chicken, Aves labs GFP 1010, 1:200); Integrin alpha 8 (goat, R&D AF4076, 1:200); TUJj1 (rabbit, Sigma T2200, 1:1000); Keratin 8 (rat, Developmental studies hybridoma bank TROMA-I, 1:200); Synaptotagmin 1/2 (rabbit, Synaptic Systems 105003, 1:500); Synaptophysin (rabbit, Thermo Fisher Scientific MA514523, 1:100); Smooth Muscle Actin (rabbit, Abcam ab5694, 1:800 or mouse, anti-SMA-Cy3, Sigma C6198, 1:300); CD31 (rat, Abcam ab56299, 1:100 or rat, BD Biosciences 550274, 1:50); Nephronectin/NPNT (goat, R&D System AF4298, 1:200); HA antibody (rabbit, Cell Signaling 3724s, 1:200); Vesicular monoamine transporter 2 (rabbit, Synaptic Systems 138313, 1:500); SOX9 (rabbit, EMD Millipore AB5535, 1:500); Keratin 82 (guinea pig, ORIGENE BP5091, 1:200); GATA3 (rat, Thermo Fisher Scientific 14–9966-80, 1:100); Keratin 6 (rabbit, BioLegend 905702 / Covance PRB-169P, 1:1000); CD140a (goat, R&D Systems AF1062-SP, 1:200); tdTomato (rat, Kerafast EST203, 1:500); Beta galactosidase (rabbit, MP Bio 559761, 1:2500); and Keratin 14 (rabbit, BioLegened PRB-155P, 1:800). For c-FOS staining, sympathetic ganglia chain was freshly embedded in OCT. 40-μm thick sections were fixed in 2% PFA for 5 minutes, washed in 0.3% Triton in PBS, and incubated with 0.1 M glycine for 5 minutes. Slides were then washed, blocked (5% Donkey serum; 1% BSA, 2% Cold water fish gelatin, and 0.3% Triton in PBS) for 1 – 4 hours at room temperature, incubated with primary c-FOS antibody (rabbit, Abcam ab190289, 1:2000) overnight at 4°C, and then incubated with secondary antibody for 2 – 4 hours at room temperature or overnight at 4°C. For nuclear counter staining, samples were incubated in 1 μg/ml DAPI (Sigma) for 2 – 4 hours at room temperature or overnight at 4°C. EdU was developed for 1 hour, using the Click-It reaction according to the manufacturer's instructions (Thermo Fisher Scientific). Hematoxylin and Eosin (H&E) staining and Masson's staining were performed according to standard protocols with the following timing modifications for early postnatal samples: For Masson's trichrome staining, 20-μm sections were incubated in Weigert's iron hematoxylin (Solution A+B) for 2 minutes, in scarlet acid solution for 3 minutes, and in aniline blue solution for 1.5 minutes. For H&E, 20 – 50-μm thick sections were incubated for 2 minutes in hematoxylin and 3 minutes in eosin solutions.

FACS—FACS was used to isolate first telogen HFSCs in control and *K15-CrePGR; Adrb2 fl/fl* male mice. Mouse back skin was dissected, and the fat layer was scraped using a surgical scalpel. The skin was incubated in trypsin-EDTA at 37°C for 35 – 45 minutes on an orbital shaker. Single cell suspension was obtained by scraping the epidermal side and filtering through 70-μm and 40-μm filters. Single cell suspensions were then centrifuged for 8 minutes at 350g at 4°C, resuspended in 5% FBS and stained for 30 – 45 minutes. The following antibodies were used: CD49f-PE-Integrin alpha 6 (eBioscience 12–0495-82, 1:500); CD34-eF660 (eBioscience 500341–82, 1:100); Ly-6A/E (Sca-1)-PerCp-Cy5.5 (eBioscience 45–5981-82, 1:1000); and CD45-eF450 (eBioscience 48–0451-82, 1:250).

DAPI (Sigma) was used to exclude dead cells. HFSCs were isolated as CD45 negative, Integrin alpha 6+, CD34+, Sca-1 negative cells. Cell isolation was performed with BD-Aria sorters.

RNA isolation—First telogen HFSCs from control and *K15-CrePGR; Adrb2 fl/fl* male mice were FACS sorted and collected into TRIzol® LS Reagent (Invitrogen). RNA was isolated with an RNeasy Micro Kit (Qiagen), using a QIAcube according to the manufacturer's instructions. RNA concentration and RNA integrity were determined by Bioanalyzer (Agilent, Santa Clara, CA) using the RNA 6000 Nano chip. High quality RNA samples with RNA Integrity Number ≥ 8 were used as input for RT-PCR and RNA-sequencing. For *Shh*, *Dhh*, and *Ihh* quantitative real time PCR, newborn pups were used. The mouse back skin was dissected. The skin was incubated with 0.25% Collagenase (Sigma c2674) in Hank's Balanced Salt Solution (HBSS) at 37°C for 20 – 35 minutes on an orbital shaker. The dermal side was scraped, and cells were collected and incubated for 10 minutes in trypsin-EDTA at 37°C to generate a single cell suspension. The remaining tissue was incubated in trypsin-EDTA at 37°C and scraped again. All cells were collected together and filtered through 70-μm and 40-μm filters. Single cell suspensions were then centrifuged for 8 minutes at 350g at 4°C and re-suspended in TRIzol® LS Reagent (Invitrogen). RNA isolation was performed using ZYMO RESEARCH Direct-Zol RNA Micro-Prep kit (zr2060) according to the manufacturer's protocol.

Quantitative real-time PCR—The cDNA libraries were synthesized using Superscript IV VILO master mix with ezDNase (Thermo Fisher). Quantitative real time PCR was performed using power SYBR green (Thermo Fisher). Ct values were normalized to beta-actin.

Primer:	Sequence:
Adrb2-set1-forward	TGGGGCCAGTCACATCCTTAT
Adrb2-set1-reverse	TGACGCACAACACATCAATGG
Adrb2-set2-forward	TACACAGGGGAGCCAAACAC
Adrb2-set2-reverse	TCACAAAGCCTTCCATGCCT
B-actin forward	CCTGTATGCCTCTGGTCGTA
B-actin reverse	CCATCTCCTGCTCGAAGTCT
Foxp1-forward	GTCTTGTGGCGTTCTGCA
Foxp1-reverse	GCTGGACCCGTTCTGGAT
Fgf18-forward	CCCAGGACTTGAATGTGCTT
Fgf18-reverse	ACTGCTGTGCTTCCAGGTTC
Shh-forward	GGGACCGCAGCAAGTACGGC
Shh-reverse	CGGATTTGGCCGCCACGGAG
Dhh-forward	GGTAACAAGGGGGTCGGAG
Dhh-reverse	TTGCAACGCTCTGTCATCAG
Ihh-forward	CTCTTGCCTACAAGCAGTTCA

Primer:	Sequence:
Ihh-reverse	CCGTGTTCTCCTCGTCCTT

RNA-sequencing and analysis—RNA-sequencing libraries were prepared using 1 ng of total RNA as input. SMART-Seq v4 Ultra Low Input RNA Kit for Sequencing (Takara) was used for cDNA synthesis, with a 10 cycle PCR enrichment. Sequencing libraries were then made using Illumina's Nextera XT Library Prep kit. A modified quarter-volume reaction protocol was used for both kits. The indexed libraries were sequenced over two flow cells on a NextSeq High-Output platform using the unpaired, 75-bp read-length sequencing protocol to obtain a total of at least 10 million reads per sample.

Sequencing reads were aligned to the mouse genome (mm10) using Salmon (Patro et al., 2017). Differential expression analysis was performed using DESeq2 (Love et al., 2014). Statistical significance was given to genes using adjusted P value of 0.1 according to Benjamini-Hochberg adjustment with FDR=0.1 and absolute fold change bigger than 2. Pathway analyses were performed using Ingenuity Pathway Analysis (IPA-QIAGEN) and Gene Ontology (GO) for the statistically significant genes. Heatmaps were generated using TPM values of all sequenced genes. The accession number for RNA-sequencing raw and analyzed data in GEO is GSE130240.

Hair cycle staging—H&E stained sections were used for analysis. For quantification, anagen II and anagen III were considered as early anagen, anagen IV was mid anagen, and anagen V and anagen VI were full anagen. Hair cycle stages were determined using previously described criteria (Muller-Rover et al., 2001). Ten to twenty hair follicles were individually assessed and staged in each animal, and at least 4 different animals were used per condition. Hair cycle staging in control and sympathectomized (6-OHDA injected and *TH-CreER; Rosa-lsl-attenuated DTA* mice) mice was performed on sections from the treated (6-OHDA injected or treated with 4-Hydroxytamoxifen) area at P30-P34. For comparison, 6-OHDA and vehicle were always injected in the same position of the back skin. For hair cycle staging of *Adrb2*-cKO mice, a biopsy was taken from similar anatomical locations in control and *Adrb2*-cKO (only males were used for the analysis). Hair cycle staging in control and AAV8-CAG-FGF18–3XHA injected mice was performed on sections from the injected site. Hair cycle staging in sham and ADX+CORT mice was perform on dorsal skin sections. Only animals with comparable plasma corticosterone levels were used (as measured by ELISA). The effects of cold exposure and adrenergic agonist treatment (isoproterenol and procaterol) on anagen entry were quantified by monitoring the change of hair regrowth as previously described (Fan et al., 2018; Sheen et al., 2015). The percent of dorsal skin in anagen was quantified using Fiji. For all analyses, sex- and aged-matched mice were used.

Electron microscopy—P21 back skin was dissected and fixed using 4% PFA, 2.5% glutaraldehyde in 0.1 M sodium cacodylate buffer. Samples were submitted for further processing (staining, embedding, sectioning, and imaging) to Renovo Neural Inc. (Cleveland) for serial section TEM (80 nM per slice, 8 – 10 nM per pixel). Three

independent hair follicles were analyzed. For 3D analysis, EM images were manually segmented and rendered using VAST lite. To visualize neurotransmitter positive vesicles, skin samples were fixed in 2.5% glutaraldehyde, 1.25% paraformaldehyde, and 0.03% picric acid in 0.1 M sodium cacodylate buffer (pH 7.4), washed in 0.1 M cacodylate buffer, and post-fixed with 1% osmium tetroxide (OsO4) in 1.5% potassium ferrocyanide (KFeCN6) for 1 hour, washed twice in water, washed once in Maleate buffer (MB), incubated in 1% uranyl acetate in MB for 1 hour followed by 2 washes in water, and subsequently dehydrated in grades of alcohol (10 minutes each; 50%, 70%, 90%, 2×10 minutes 100%). The samples were then put in propyleneoxide for 1 hour and infiltrated overnight in a 1:1 mixture of propyleneoxide and Spurr's low viscosity resin (Electron Microscopy Sciences, Hatfield, PA). The following day the samples were embedded in Spurr's resin and polymerized at 60°C for 48 hours. Ultrathin sections (about 80 nm) were cut on a Reichert Ultracut-S microtome, picked up on to copper grids stained with lead citrate, and examined in a JEOL 1200EX. Transmission electron microscope images were recorded with an AMT 2k CCD camera.

RU486 treatment—For topical treatment, 4% Mifepristone (TCI America, M1732) in ethanol was used to induce *K15-CrePGR*. The dorsal skin of the mice was shaved prior to treatment. RU486 was applied topically 10 – 14 times once a day to both control and *K15-CrePGR; Adrb2 fl/fl* mice.

Adrenergic agonist topical application—Procaterol (10 mg/kg body weight, Sigma P9180) or isoproterenol (10 mg/kg body weight, Sigma I5627) were dissolved in hand cream (Neutrogena Norwegian Formula Concentrated Hand Cream) at 10 mg drug/1 g cream concentration. The dorsal skin was shaved prior to treatment. The isoproterenol/procaterol-cream was applied topically once a day for 10 days. Cream without agonists was applied to control mice.

Diphtheria toxin administration—Diphtheria toxin (Sigma-Aldrich) was dissolved in 0.9% NaCl (0.1 mg/ml). For APM ablation, 8-week-old *SMA-YFP-DTR* transgenic mice were intradermally injected with 250 ng/kg diphtheria toxin.

Imaging and image analysis—All images were acquired using a Zeiss LSM 880, LSM 700 confocal microscope, or Keyence microscope using x10, x20 or x63 magnification lenses. Images are presented as either a Maximum Intensity Projection image or a single Z stack. For image analysis, Imaris software (Oxford Instruments) and Fiji (Schindelin et al., 2012) were used. The following analyses were performed using Imaris software:

1. Co-localization between YFP and ITGA8 was quantified using the Imaris colocalization module. For each analyzed APM, a region of interest covering the entire APM was defined and used for all measurements. Seven to twelve muscles were analyzed in each animal, and 3 animals were used for analysis at all time points. Outlining of the APM was performed according to ITGA8 staining for both channels. For YFP and ITGA8 co-localization, the value of "% of material above threshold colocalized" was used.

2. Quantification of SMA+ blood vessels. First a CD31+ volume was automatically created. Using the “distance transformation” and “mask” functions, a second SMA+ volume up to 2 μm from CD31+ cells was created. To quantify the percent of endothelial cells volume covered by SMA+, this volume (SMA+ volume, 2 μm from CD31+ staining) was divided by the total CD31+ volume and presented as a percentage. Three to seven 20x confocal images were quantified per animal. Three control and 3 *SMA-YFP-DTR* animals were used. For *Fgf18 in situ* quantification, bright field images were used. *Fgf18*+ spots in the outer bulge (HFSC) area were manually counted using Fiji. Seven to eleven hair follicles were quantified per animal, and 3 animals were used for each condition (3 control and 3 *K15-CrePGR; Adrb2 fl/fl*). For c-FOS+ quantification in sympathetic ganglia, TH and c-FOS stained sections were used. TH staining was used to identify the sympathetic ganglia. The total number of cells (TH+) as well as c-FOS+ positive cells were manually quantified using Fiji. Three to five sympathetic ganglia were quantified per animal, and 2 animals per condition (cold and control) were used. For quantification of hair follicles with APM during development, dorsal skin was used. Using Fiji, the number of hair follicles and APMs was manually counted. Results are presented as (number of APM/number of hair follicle) x 100. For innervation frequency analysis: First telogen maximum projection 20X images were used. For each hair follicle, HFSCs were divided into four compartments: upper bulge, mid bulge, lower bulge, and hair germ. For every quantified hair follicle, the innervation pattern was analyzed and each HFSC compartment was scored “1” if innervation was present or “0” if there was no innervation. Ten to thirty hair follicles were individually assessed in each animal, and 2–3 different animals were used for quantification.

Analysis of published datasets—For RNA-seq data of adrenergic receptors, the following datasets were used: Ge Y et al., 2017, GEO accession GSE89928 and Lay et al., 2016 PNAS, GEO accession GSE77256. For ChIP-seq of adrenergic receptors the following dataset was used: Lien WH, 2011 Cell Stem Cell, GEO accession GSE31239.

Quantification and Statistical Analysis—Statistical analyses were performed with Prism using unpaired two-tailed Student’s t-test. Statistical significance is denoted by asterisks ($P<0.05$ [*], $P < 0.01$ [**], and $P < 0.0001$ [***]. The data are presented as mean ± SEM. All statistical details (including the value of n and what it represents) can be found in figures and figure legends.

Supplementary Material

Refer to Web version on PubMed Central for supplementary material.

ACKNOWLEDGEMENTS

We thank G. Karsenty for *Adrb2 fl/fl* mice, D. Ginty, C. Harwell, and L. Orefice for the *Avil-Cre; Shh fl/fl* mice, and many colleagues who donated mice to JAX; Y. Fong, C. Huang, D. Ginty, L. Orefice, X. Jin for comments on the manuscript, N. Alharbi, S. Kim, S. Tham, Y.-L. Kang, HCBI, HSCRB FACS core, HMS EM facility, and

HSCRB histology core for technical support; A. Shwartz for assistance with imaging analyses; G. Kidd and E. Benson for block face scanning EM; Transgenic Mouse Core Lab, National Taiwan University Centers of Genomic and Precision Medicine for generation of the SMA-YFP-DTR transgenic mouse line. This work was supported by the New York Stem Cell Foundation, the Smith Family Foundation Odyssey Award, the Pew Charitable Trusts, Harvard NeuroDiscovery Center, Harvard Stem Cell Institute, Harvard Medical School Dean's Innovation Grant, American Cancer Society (RSG-18–152-01DDC), NIH (R01-AR070825 to Y.-C.H.; R01DK077097 and R01DK102898 to Y.-H. T.), Taiwan Ministry of Science and Technology (107–2314-B-002–064-MY3 to S.-J.L.), and National Taiwan University Hospital (UN107–005, 107S3781, UN108–029, UN109–005 to S.-J.L.). Y.-C.H. is a Pew Scholar and a NYSCF – Robertson Investigator. Y.S. is a Helen Hay Whitney postdoctoral fellow and receives the Woman in Science Weizmann Institute of Science Award. M.G.-C. and M.H. are recipients of the Simmons Family Award. F.S. is supported by the American Diabetes Association grant (1–18-PDF-169). B.Z. is awarded with the Charles A. King Trust Postdoctoral Research Fellowship. M.H is supported by the NSF Graduate Research Fellowships Program (DGE1745303).

REFERENCE

Abraira VE, Kuehn ED, Chirila AM, Springel MW, Toliver AA, Zimmerman AL, Orefice LL, Boyle KA, Bai L, Song BJ, et al. (2017). The Cellular and Synaptic Architecture of the Mechanosensory Dorsal Horn. Cell 168, 295–310 e219. [PubMed: 28041852]

Andl T, Reddy ST, Gaddapara T, and Millar SE (2002). WNT signals are required for the initiation of hair follicle development. Dev Cell 2, 643–653. [PubMed: 12015971]

Asada-Kubota M. (1995). Inhibition of hair growth by subcutaneous injection of a sympathetic neurotoxin, 6-hydroxydopamine in neonatal mice. Anat Embryol (Berl) 191, 407–414. [PubMed: 7625611]

Bai CB, Auerbach W, Lee JS, Stephen D, and Joyner AL (2002). Gli2, but not Gli1, is required for initial Shh signaling and ectopic activation of the Shh pathway. Development 129, 4753–4761. [PubMed: 12361967]

Belteki G, Haigh J, Kabacs N, Haigh K, Sison K, Costantini F, Whitsett J, Quaggin SE, and Nagy A. (2005). Conditional and inducible transgene expression in mice through the combinatorial use of Cre-mediated recombination and tetracycline induction. Nucleic Acids Res 33, e51. [PubMed: 15784609]

Bitgood MJ, Shen L, and McMahon AP (1996). Sertoli cell signaling by Desert hedgehog regulates the male germline. Curr Biol 6, 298–304. [PubMed: 8805249]

Borden P, Houtz J, Leach SD, and Kuruvilla R. (2013). Sympathetic innervation during development is necessary for pancreatic islet architecture and functional maturation. Cell Rep 4, 287–301. [PubMed: 23850289]

Botchkarev VA, Peters EM, Botchkareva NV, Maurer M, and Paus R. (1999). Hair cycledependent changes in adrenergic skin innervation, and hair growth modulation by adrenergic drugs. J Invest Dermatol 113, 878–887. [PubMed: 10594725]

Brownell I, Guevara E, Bai CB, Loomis CA, and Joyner AL (2011). Nerve-derived sonic hedgehog defines a niche for hair follicle stem cells capable of becoming epidermal stem cells. Cell Stem Cell 8, 552–565. [PubMed: 21549329]

Burnstock G. (2008). Non-synaptic transmission at autonomic neuroeffector junctions. Neurochem Int 52, 14–25. [PubMed: 17493707]

Chen CL, Huang WY, Wang EHC, Tai KY, and Lin SJ (2020). Functional complexity of hair follicle stem cell niche and therapeutic targeting of niche dysfunction for hair regeneration. J Biomed Sci 27, 43. [PubMed: 32171310]

Chiang C, Swan RZ, Grachtchouk M, Bolinger M, Litingtung Y, Robertson EK, Cooper MK, Gaffield W, Westphal H, Beachy PA, et al. (1999). Essential role for Sonic hedgehog during hair follicle morphogenesis. Dev Biol 205, 1–9. [PubMed: 9882493]

Crowe R, Mitsou J, McGrouther DA, and Burnstock G. (1993). An increase in the growth of hair associated with hyperinnervation of the underlying vessels in rabbit skin. Neurosci Lett 161, 105–108. [PubMed: 8255535]

Darwin CR (1872). The expression of the emotions in man and animals (London: John Murray).

Dassule HR, Lewis P, Bei M, Maas R, and McMahon AP (2000). Sonic hedgehog regulates growth and morphogenesis of the tooth. Development 127, 4775–4785. [PubMed: 11044393]

Driskell RR, Lichtenberger BM, Hoste E, Kretzschmar K, Simons BD, Charalambous M, Ferron SR, Herault Y, Pavlovic G, Ferguson-Smith AC, et al. (2013). Distinct fibroblast lineages determine dermal architecture in skin development and repair. Nature 504, 277–281. [PubMed: 24336287]

Fan SM, Chang YT, Chen CL, Wang WH, Pan MK, Chen WP, Huang WY, Xu Z, Huang HE, Chen T, et al. (2018). External light activates hair follicle stem cells through eyes via an ipRGC-SCN-sympathetic neural pathway. Proc Natl Acad Sci U S A 115, E6880–E6889. [PubMed: 29959210]

Fujiwara H, Ferreira M, Donati G, Marciano DK, Linton JM, Sato Y, Hartner A, Sekiguchi K, Reichardt LF, and Watt FM (2011). The basement membrane of hair follicle stem cells is a muscle cell niche. Cell 144, 577–589. [PubMed: 21335239]

Furlan A, La Manno G, Lubke M, Haring M, Abdo H, Hochgerner H, Kupari J, Usoskin D, Airaksinen MS, Oliver G, et al. (2016). Visceral motor neuron diversity delineates a cellular basis for nipple- and pilo-erection muscle control. Nat Neurosci 19, 1331–1340. [PubMed: 27571008]

Ge Y, Gomez NC, Adam RC, Nikolova M, Yang H, Verma A, Lu CP, Polak L, Yuan S, Elemento O, et al. (2017). Stem Cell Lineage Infidelity Drives Wound Repair and Cancer. Cell 169, 636–650 e614. [PubMed: 28434617]

Goldstein JM, Tabebordbar M, Zhu K, Wang LD, Messemer KA, Peacker B, Ashrafi Kakhki S, Gonzalez-Celeiro M, Shwartz Y, Cheng JKW, et al. (2019). In Situ Modification of Tissue Stem and Progenitor Cell Genomes. Cell Rep 27, 1254–1264 e1257. [PubMed: 31018138]

Greco V, Chen T, Rendl M, Schober M, Pasolli HA, Stokes N, Dela Cruz-Racelis J, and Fuchs E. (2009). A two-step mechanism for stem cell activation during hair regeneration. Cell Stem Cell 4, 155–169. [PubMed: 19200804]

Heidt T, Sager HB, Courties G, Dutta P, Iwamoto Y, Zaltsman A, von Zur Muhlen C, Bode C, Fricchione GL, Denninger J, et al. (2014). Chronic variable stress activates hematopoietic stem cells. Nat Med 20, 754–758. [PubMed: 24952646]

Heitman N, Sennett R, Mok KW, Saxena N, Srivastava D, Martino P, Grisanti L, Wang Z, Ma'ayan A, Rompolas P, et al. (2020). Dermal sheath contraction powers stem cell niche relocation during hair cycle regression. Science 367, 161–166. [PubMed: 31857493]

Hinoi E, Gao N, Jung DY, Yadav V, Yoshizawa T, Myers MG Jr., Chua SC Jr., Kim JK, Kaestner KH, and Karsenty G. (2008). The sympathetic tone mediates leptin's inhibition of insulin secretion by modulating osteocalcin bioactivity. J Cell Biol 183, 1235–1242. [PubMed: 19103808]

Hsu YC, Li L, and Fuchs E. (2014a). Emerging interactions between skin stem cells and their niches. Nat Med 20, 847–856. [PubMed: 25100530]

Hsu YC, Li L, and Fuchs E. (2014b). Transit-amplifying cells orchestrate stem cell activity and tissue regeneration. Cell 157, 935–949. [PubMed: 24813615]

Hsu YC, Pasolli HA, and Fuchs E. (2011). Dynamics between stem cells, niche, and progeny in the hair follicle. Cell 144, 92–105. [PubMed: 21215372]

Kamiya A, Hayama Y, Kato S, Shimomura A, Shimomura T, Irie K, Kaneko R, Yanagawa Y, Kobayashi K, and Ochiya T. (2019). Genetic manipulation of autonomic nerve fiber innervation and activity and its effect on breast cancer progression. Nat Neurosci 22, 1289–1305. [PubMed: 31285612]

Karemaker JM (2017). An introduction into autonomic nervous function. Physiol Meas 38, R89–R118. [PubMed: 28304283]

Katayama Y, Battista M, Kao WM, Hidalgo A, Peired AJ, Thomas SA, and Frenette PS (2006). Signals from the sympathetic nervous system regulate hematopoietic stem cell egress from bone marrow. Cell 124, 407–421. [PubMed: 16439213]

Kimura-Ueki M, Oda Y, Oki J, Komi-Kuramochi A, Honda E, Asada M, Suzuki M, and Imamura T. (2012). Hair cycle resting phase is regulated by cyclic epithelial FGF18 signaling. J Invest Dermatol 132, 1338–1345. [PubMed: 22297635]

Kobayasi S, Okuyama F, and Takagi K. (1958). Experimental studies on the hemitrichosis and the nervous influences on the hair growth. Acta Neuroveg (Wien) 18, 169–190. [PubMed: 13616959]

Kong Y, Liu Y, Pan L, Cheng B, and Liu H. (2015). Norepinephrine Regulates Keratinocyte Proliferation to Promote the Growth of Hair Follicles. Cells Tissues Organs 201, 423–435. [PubMed: 27286967]

Kostrzewa RM, and Jacobowitz DM (1974). Pharmacological actions of 6-hydroxydopamine. Pharmacol Rev 26, 199–288. [PubMed: 4376244]

Lay K, Kume T, and Fuchs E. (2016). FOXC1 maintains the hair follicle stem cell niche and governs stem cell quiescence to preserve long-term tissue-regenerating potential. Proc Natl Acad Sci U S A 113, E1506–1515. [PubMed: 26912458]

Leishman E, Howard JM, Garcia GE, Miao Q, Ku AT, Dekker JD, Tucker H, and Nguyen H. (2013). Foxp1 maintains hair follicle stem cell quiescence through regulation of Fgf18. Development 140, 3809–3818. [PubMed: 23946441]

Lewis PM, Dunn MP, McMahon JA, Logan M, Martin JF, St-Jacques B, and McMahon AP (2001). Cholesterol modification of sonic hedgehog is required for long-range signaling activity and effective modulation of signaling by Ptc1. Cell 105, 599–612. [PubMed: 11389830]

Li L, and Ginty DD (2014). The structure and organization of lanceolate mechanosensory complexes at mouse hair follicles. Elife 3, e01901. [PubMed: 24569481]

Lien WH, Guo X, Polak L, Lawton LN, Young RA, Zheng D, and Fuchs E. (2011). Genome-wide maps of histone modifications unwind in vivo chromatin states of the hair follicle lineage. Cell Stem Cell 9, 219–232. [PubMed: 21885018]

Llorens-Bobadilla E, Zhao S, Baser A, Saiz-Castro G, Zwadlo K, and Martin-Villalba A. (2015). Single-Cell Transcriptomics Reveals a Population of Dormant Neural Stem Cells that Become Activated upon Brain Injury. Cell Stem Cell 17, 329–340. [PubMed: 26235341]

Long F, Zhang XM, Karp S, Yang Y, and McMahon AP (2001). Genetic manipulation of hedgehog signaling in the endochondral skeleton reveals a direct role in the regulation of chondrocyte proliferation. Development 128, 5099–5108. [PubMed: 11748145]

Love MI, Huber W, and Anders S. (2014). Moderated estimation of fold change and dispersion for RNA-seq data with DESeq2. Genome Biol 15, 550. [PubMed: 25516281]

Lucas D, Scheiermann C, Chow A, Kunisaki Y, Bruns I, Barrick C, Tessarollo L, and Frenette PS (2013). Chemotherapy-induced bone marrow nerve injury impairs hematopoietic regeneration. Nat Med 19, 695–703. [PubMed: 23644514]

Maryanovich M, Zahalka AH, Pierce H, Pinho S, Nakahara F, Asada N, Wei Q, Wang X, Ciero P, Xu J, et al. (2018). Adrenergic nerve degeneration in bone marrow drives aging of the hematopoietic stem cell niche. Nat Med 24, 782–791. [PubMed: 29736022]

Morris RJ, Liu Y, Marles L, Yang Z, Trempus C, Li S, Lin JS, Sawicki JA, and Cotsarelis G. (2004). Capturing and profiling adult hair follicle stem cells. Nat Biotechnol 22, 411–417. [PubMed: 15024388]

Mou H, Vinarsky V, Tata PR, Brazauskas K, Choi SH, Crooke AK, Zhang B, Solomon GM, Turner B, Bihler H, et al. (2016). Dual SMAD Signaling Inhibition Enables Long-Term Expansion of Diverse Epithelial Basal Cells. Cell Stem Cell 19, 217–231. [PubMed: 27320041]

Muller-Rover S, Handjiski B, van der Veen C, Eichmuller S, Foitzik K, McKay IA, Stenn KS, and Paus R. (2001). A comprehensive guide for the accurate classification of murine hair follicles in distinct hair cycle stages. J Invest Dermatol 117, 3–15. [PubMed: 11442744]

Nowak JA, and Fuchs E. (2009). Isolation and culture of epithelial stem cells. Methods Mol Biol 482, 215–232. [PubMed: 19089359]

Oshima H, Rochat A, Kedzia C, Kobayashi K, and Barrandon Y. (2001). Morphogenesis and renewal of hair follicles from adult multipotent stem cells. Cell 104, 233–245. [PubMed: 11207364]

Patro R, Duggal G, Love MI, Irizarry RA, and Kingsford C. (2017). Salmon provides fast and bias-aware quantification of transcript expression. Nat Methods 14, 417–419. [PubMed: 28263959]

Perdigoto CN, Dauber KL, Bar C, Tsai PC, Valdes VJ, Cohen I, Santoriello FJ, Zhao D, Zheng D, Hsu YC, et al. (2016). Polycomb-Mediated Repression and Sonic Hedgehog Signaling Interact to Regulate Merkel Cell Specification during Skin Development. PLoS Genet 12, e1006151. [PubMed: 27414999]

Peters EM, Maurer M, Botchkarev VA, Gordon DS, and Paus R. (1999). Hair growthmodulation by adrenergic drugs. Exp Dermatol 8, 274–281. [PubMed: 10439225]

Peterson SC, Eberl M, Vagnozzi AN, Belkadi A, Veniaminova NA, Verhaegen ME, Bichakjian CK, Ward NL, Dlugosz AA, and Wong SY (2015). Basal cell carcinoma preferentially arises from stem

cells within hair follicle and mechanosensory niches. Cell Stem Cell 16, 400–412. [PubMed: 25842978]

Pruitt SC, Freeland A, Rusiniak ME, Kunnev D, and Cady GK (2013). Cdkn1b overexpression in adult mice alters the balance between genome and tissue ageing. Nat Commun 4, 2626. [PubMed: 24149709]

Rezza A, Wang Z, Sennett R, Qiao W, Wang D, Heitman N, Mok KW, Clavel C, Yi R, Zandstra P, et al. (2016). Signaling Networks among Stem Cell Precursors, TransitAmplifying Progenitors, and their Niche in Developing Hair Follicles. Cell Rep 14, 3001–3018. [PubMed: 27009580]

Rivera-Gonzalez GC, Shook BA, Andrae J, Holtrup B, Bollag K, Betsholtz C, Rodeheffer MS, and Horsley V. (2016). Skin Adipocyte Stem Cell Self-Renewal Is Regulated by a PDGFA/AKT-Signaling Axis. Cell Stem Cell 19, 738–751. [PubMed: 27746098]

Rochat A, Kobayashi K, and Barrandon Y. (1994). Location of stem cells of human hair follicles by clonal analysis. Cell 76, 1063–1073. [PubMed: 8137423]

Rodgers JT, King KY, Brett JO, Cromie MJ, Charville GW, Maguire KK, Brunson C, Mastey N, Liu L, Tsai CR, et al. (2014). mTORC1 controls the adaptive transition of quiescent stem cells from G0 to G(Alert). Nature 510, 393–396. [PubMed: 24870234]

Roesch K, Jadhav AP, Trimarchi JM, Stadler MB, Roska B, Sun BB, and Cepko CL (2008). The transcriptome of retinal Muller glial cells. J Comp Neurol 509, 225–238. [PubMed: 18465787]

Rompolas P, Mesa KR, and Greco V. (2013). Spatial organization within a niche as a determinant of stem-cell fate. Nature 502, 513–518. [PubMed: 24097351]

Rompolas P, Mesa KR, Kawaguchi K, Park S, Gonzalez D, Brown S, Boucher J, Klein AM, and Greco V. (2016). Spatiotemporal coordination of stem cell commitment during epidermal homeostasis. Science 352, 1471–1474. [PubMed: 27229141]

Sada A, Jacob F, Leung E, Wang S, White BS, Shalloway D, and Tumbar T. (2016). Defining the cellular lineage hierarchy in the interfollicular epidermis of adult skin. Nat Cell Biol 18, 619–631. [PubMed: 27183471]

Schindelin J, Arganda-Carreras I, Frise E, Kaynig V, Longair M, Pietzsch T, Preibisch S, Rueden C, Saalfeld S, Schmid B, et al. (2012). Fiji: an open-source platform for biological-image analysis. Nat Methods 9, 676–682. [PubMed: 22743772]

Schmidt-Ullrich R, and Paus R. (2005). Molecular principles of hair follicle induction and morphogenesis. Bioessays 27, 247–261. [PubMed: 15714560]

Sennett R, Wang Z, Rezza A, Grisanti L, Roitershtein N, Sicchio C, Mok KW, Heitman NJ, Clavel C, Ma'ayan A, et al. (2015). An Integrated Transcriptome Atlas of Embryonic Hair Follicle Progenitors, Their Niche, and the Developing Skin. Dev Cell 34, 577–591. [PubMed: 26256211]

Sheen YS, Fan SM, Chan CC, Wu YF, Jee SH, and Lin SJ (2015). Visible red light enhances physiological anagen entry in vivo and has direct and indirect stimulative effects in vitro. Lasers Surg Med 47, 50–59. [PubMed: 25557083]

Sheu SH, Tapia JC, Tsuriel S, and Lichtman JW (2017). Similar synapse elimination motifs at successive relays in the same efferent pathway during development in mice. Elife 6, e23193. [PubMed: 28157072]

Srinivas S, Watanabe T, Lin CS, William CM, Tanabe Y, Jessell TM, and Costantini F. (2001). Cre reporter strains produced by targeted insertion of EYFP and ECFP into the ROSA26 locus. BMC Dev Biol 1, 4. [PubMed: 11299042]

St-Jacques B, Dassule HR, Karavanova I, Botchkarev VA, Li J, Danielian PS, McMahon JA, Lewis PM, Paus R, and McMahon AP (1998). Sonic hedgehog signaling is essential for hair development. Curr Biol 8, 1058–1068. [PubMed: 9768360]

Suo D, Park J, Young S, Makita T, and Deppmann CD (2015). Coronin-1 and calcium signaling governs sympathetic final target innervation. J Neurosci 35, 3893–3902. [PubMed: 25740518]

Swanson LW, and Lichtman JW (2016). From Cajal to Connectome and Beyond. Annu Rev Neurosci 39, 197–216. [PubMed: 27442070]

Torkamani N, Rufaut NW, Jones L, and Sinclair R. (2014). Destruction of the arrector pili muscle and fat infiltration in androgenic alopecia. Br J Dermatol 170, 1291–1298. [PubMed: 24579818]

van Velthoven CTJ, de Morree A, Egner IM, Brett JO, and Rando TA (2017). Transcriptional Profiling of Quiescent Muscle Stem Cells In Vivo. Cell Rep 21, 1994–2004. [PubMed: 29141228]

Venkataramani V, Tanev DI, Strahle C, Studier-Fischer A, Fankhauser L, Kessler T, Korber C, Kardorff M, Ratliff M, Xie R, et al. (2019). Glutamatergic synaptic input to glioma cells drives brain tumour progression. Nature 573, 532–538. [PubMed: 31534219]

Venkatesh HS, Morishita W, Geraghty AC, Silverbush D, Gillespie SM, Arzt M, Tam LT, Espenel C, Ponnuswami A, Ni L, et al. (2019). Electrical and synaptic integration of glioma into neural circuits. Nature 573, 539–545. [PubMed: 31534222]

Voehringer D, Liang HE, and Locksley RM (2008). Homeostasis and effector function of lymphopenia-induced “memory-like” T cells in constitutively T cell-depleted mice. J Immunol 180, 4742–4753. [PubMed: 18354198]

Wang L, Siegenthaler JA, Dowell RD, and Yi R. (2016). Foxc1 reinforces quiescence in self-renewing hair follicle stem cells. Science 351, 613–617. [PubMed: 26912704]

Wirth A, Benyo Z, Lukasova M, Leutgeb B, Wettschureck N, Gorbey S, Orsy P, Horvath B, Maser-Gluth C, Greiner E, et al. (2008). G12-G13-LARG-mediated signaling in vascular smooth muscle is required for salt-induced hypertension. Nat Med 14, 64–68. [PubMed: 18084302]

Woo WM, Zhen HH, and Oro AE (2012). Shh maintains dermal papilla identity and hair morphogenesis via a Noggin-Shh regulatory loop. Genes Dev 26, 1235–1246. [PubMed: 22661232]

Wu S, Wu Y, and Capecchi MR (2006). Motoneurons and oligodendrocytes are sequentially generated from neural stem cells but do not appear to share common lineage-restricted progenitors in vivo. Development 133, 581–590. [PubMed: 16407399]

Wu Z, Autry AE, Bergan JF, Watabe-Uchida M, and Dulac CG (2014). Galanin neurons in the medial preoptic area govern parental behaviour. Nature 509, 325–330. [PubMed: 24828191]

Xiao Y, Thoresen DT, Miao L, Williams JS, Wang C, Atit RP, Wong SY, and Brownell I. (2016). A Cascade of Wnt, Eda, and Shh Signaling Is Essential for Touch Dome Merkel Cell Development. PLoS Genet 12, e1006150. [PubMed: 27414798]

Yazdabadi A, Whiting D, Rufaut N, and Sinclair R. (2012). Miniaturized Hairs Maintain Contact with the Arrector Pili Muscle in Alopecia Areata but not in Androgenetic Alopecia: A Model for Reversible Miniaturization and Potential for Hair Regrowth. Int J Trichology 4, 154–157. [PubMed: 23180923]

Zahalka AH, Arnal-Estape A, Maryanovich M, Nakahara F, Cruz CD, Finley LWS, and Frenette PS (2017). Adrenergic nerves activate an angio-metabolic switch in prostate cancer. Science 358, 321–326. [PubMed: 29051371]

Zhang B, and Hsu YC (2017). Emerging roles of transit-amplifying cells in tissue regeneration and cancer. Wiley Interdiscip Rev Dev Biol 6, e282.

Zhang B, Ma S, Rachmin I, He M, Baral P, Choi S, Goncalves WA, Shwartz Y, Fast EM, Su Y, et al. (2020). Hyperactivation of sympathetic nerves drives depletion of melanocyte stem cells. Nature 577, 676–681. [PubMed: 31969699]

Zhang B, Tsai PC, Gonzalez-Celeiro M, Chung O, Boumard B, Perdigoto CN, Ezhkova E, and Hsu YC (2016). Hair follicles’ transit-amplifying cells govern concurrent dermal adipocyte production through Sonic Hedgehog. Genes Dev 30, 2325–2338. [PubMed: 27807033]

Zhang YV, Cheong J, Ciapurin N, McDermitt DJ, and Tumbar T. (2009). Distinct selfrenewal and differentiation phases in the niche of infrequently dividing hair follicle stem cells. Cell Stem Cell 5, 267–278. [PubMed: 19664980]

Zurborg S, Piszczek A, Martinez C, Hublitz P, Al Banchaabouchi M, Moreira P, Perlas E, and Heppenstall PA (2011). Generation and characterization of an Advillin-Cre driver mouse line. Mol Pain 7, 66. [PubMed: 21906401]

Highlights

- The hair follicle instructs the formation of the APM-sympathetic nerve unit via SHH
- APM maintains sympathetic innervation to HFSCs
- Sympathetic nerve activates HFSCs via synapse-like contacts and norepinephrine
- Cold stimulates not only goosebumps but also hair growth

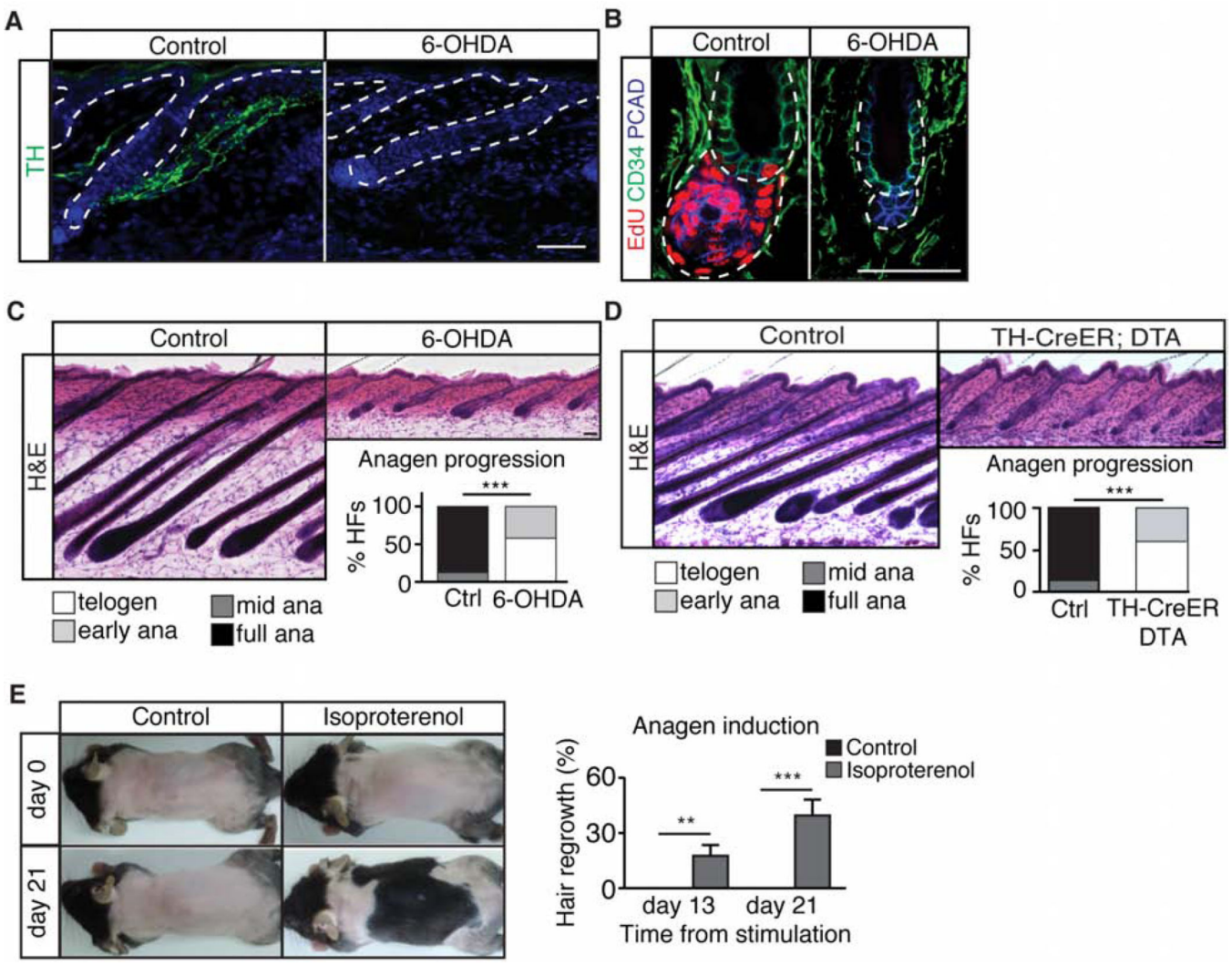

Figure 1. Sympathectomy delays anagen entry whereas elevation of sympathetic tone drives anagen entry.

(**A**) Immunofluorescent staining for tyrosine hydroxylase (TH) in control and sympathectomized (6-OHDA) skin. (**B**) Immuno-colocalization of EdU, CD34, and P-Cadherin (PCAD) in control and sympathectomized P25 skin. (**C**) Hematoxylin & Eosin (H&E) staining of control and sympathectomized skin. Graph: hair cycle distribution at P30 (n = 4 – 5 mice per condition, 20 hair follicles (HF) per mouse). (**D**) H&E staining of control and sympathectomized *TH-CreER; Rosa-lsl-attenuated DTA* (*TH-CreER; DTA*) skin. Graph: hair cycle distribution at P31 - P34 (n = 4 – 5 mice per condition, 10 HF per mouse). (**E**) Topical application of isoproterenol at the 2nd telogen results in precocious anagen entry (n = 10 mice per condition). Graph: back skin hair regrowth (%). Unless otherwise specified, all scale bars = 50 μm. Data are mean ± SEM. *: p<0.05; **: p<0.01; ***: p <0.001. See also Figure S1.

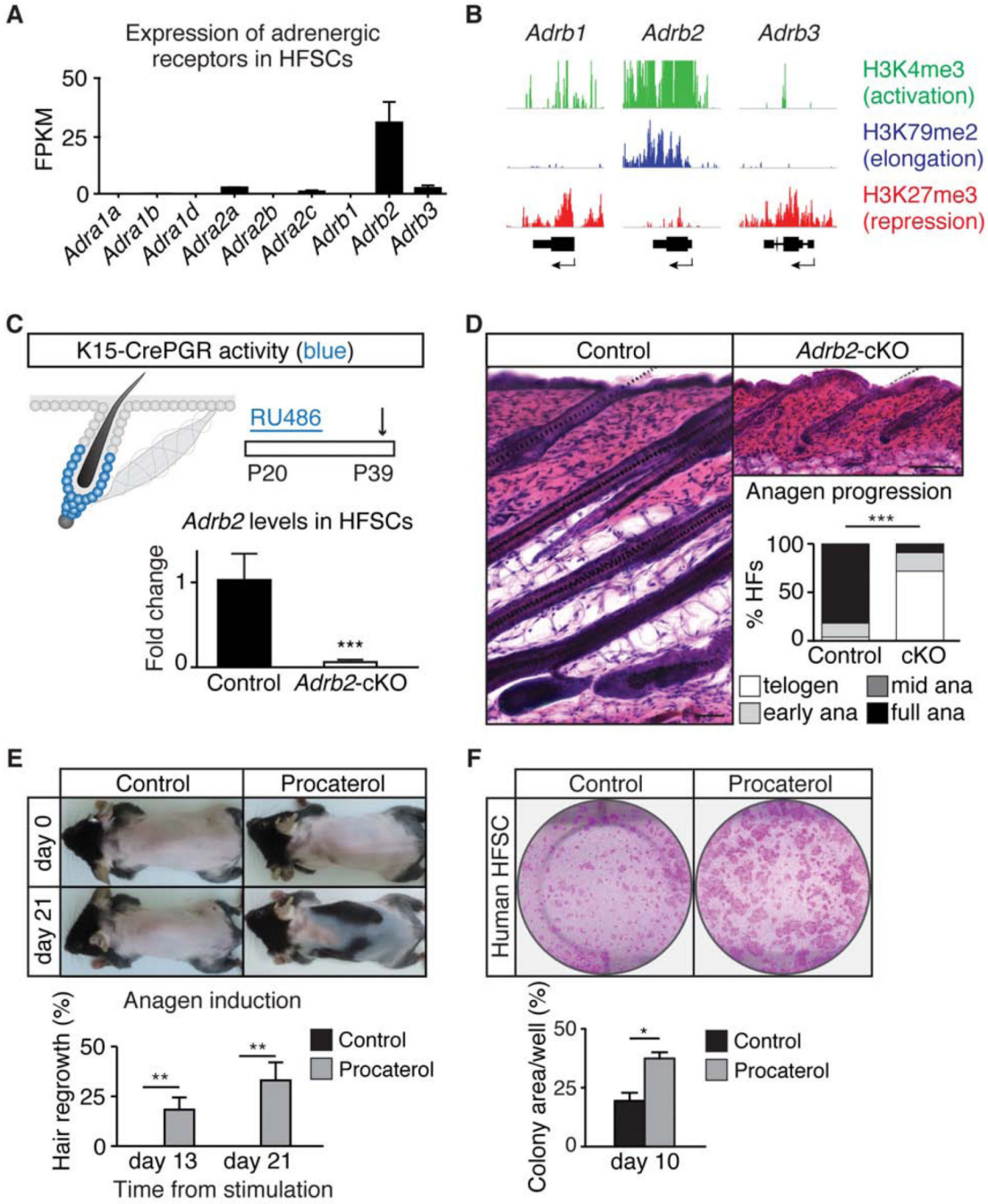

Figure 2. HFSC activity is modulated by ADRB2.

(**A**) Expression of adrenergic receptors in HFSCs (RNA-seq). (**B**) Chromatin modifications around the loci of *Adrb* genes in HFSCs. (**C**) Schematic of K15-CrePGR activity (blue) and experimental design (arrow denotes harvesting). qRT-PCR of *Adrb2* from FACS-purified HFSCs of control and *K15-CrePGR; Adrb2 fl/fl* (*Adrb2*-cKO) mice (n = 3 mice per condition). (**D**) H&E staining of control and *Adrb2*-cKO skin. Graph: hair cycle distribution (n = 5 – 7 mice per condition, 20 HF per mouse). (**E**) Topical application of procaterol (ADRB2 agonist) drives premature anagen entry (n = 10 mice per condition). Graph: back

skin hair regrowth (%). (**F**) Colony formation assay on control and procaterol-treated human HFSCs. Graph: area covered by colonies (n = 3 – 5 wells per condition). Data are mean ± SEM. *: p<0.05; **: p<0.01; ***: p <0.001. See also Figure S2.

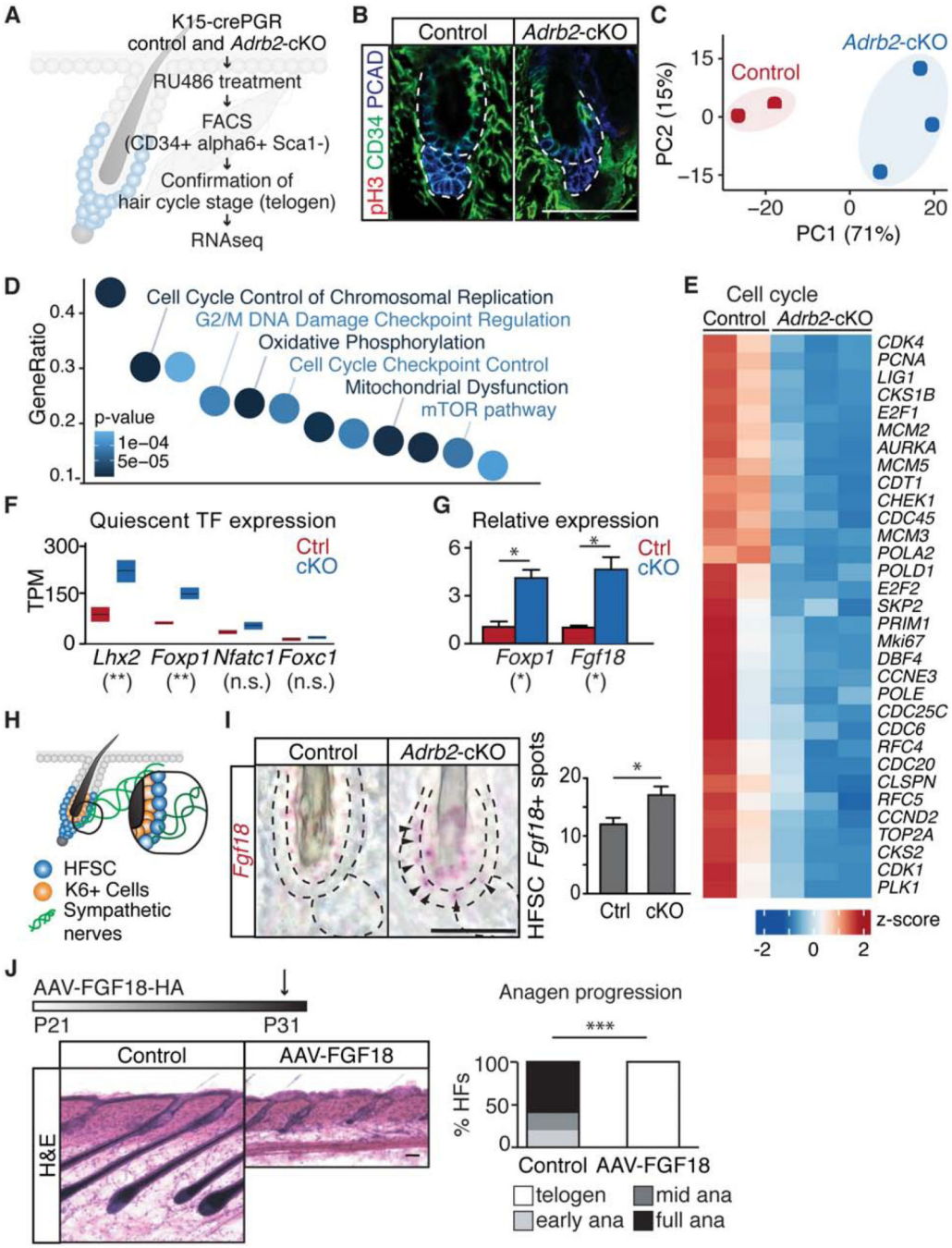

Figure 3. Transcriptome analyses of *Adrb2*-depleted HFSCs.

(**A**) Schematic of workflow. (**B**) Immunofluorescent staining for phospho-histone H3 (pH3), CD34, and PCAD in control and *Adrb2*-cKO mice. (**C**) Principal component analysis (PCA) comparing the transcriptome of control and *Adrb2*-cKO HFSCs. (**D**) Ingenuity Pathway Analysis (IPA) of significantly deregulated genes in *Adrb2*-cKO mice. (**E**) Heatmap plotting expression of cell cycle-related genes. Positive Z-score depicts higher expression; negative Z-score indicates lower expression. (**F**) Quiescent-related transcription factors in control and *Adrb2*-cKO HFSCs. High-low bar graph, line at mean. (**G**) qRT-PCR of *Foxp1* and *Fgf18*

from FACS-purified HFSCs (n = 2 – 3 mice per condition). (**H**) Schematic of bulge and sympathetic innervation (HFSCs are the outer bulge and K6+ cells are the inner bulge. Sympathetic nerve innervates only HFSCs). (**I**) *In situ* hybridization of *Fgf18* in control and *Adrb2*-cKO mice (arrowheads: positive signals in HFSCs). Graph: *Fgf18*+ signal spots in HFSCs. (**J**) H&E staining of control and AAV8-CAG-FGF18–3XHA (AAV-FGF18) injected mice. Graph: hair cycle distribution (n = 5 mice per condition, 10 HF per mouse). Scale bar, 25 μm in **I**. Data are mean ± SEM. *: $p<0.05$; **: $p<0.01$; ***: $p<0.001$; n.s.: not significant. See also Figure S3.

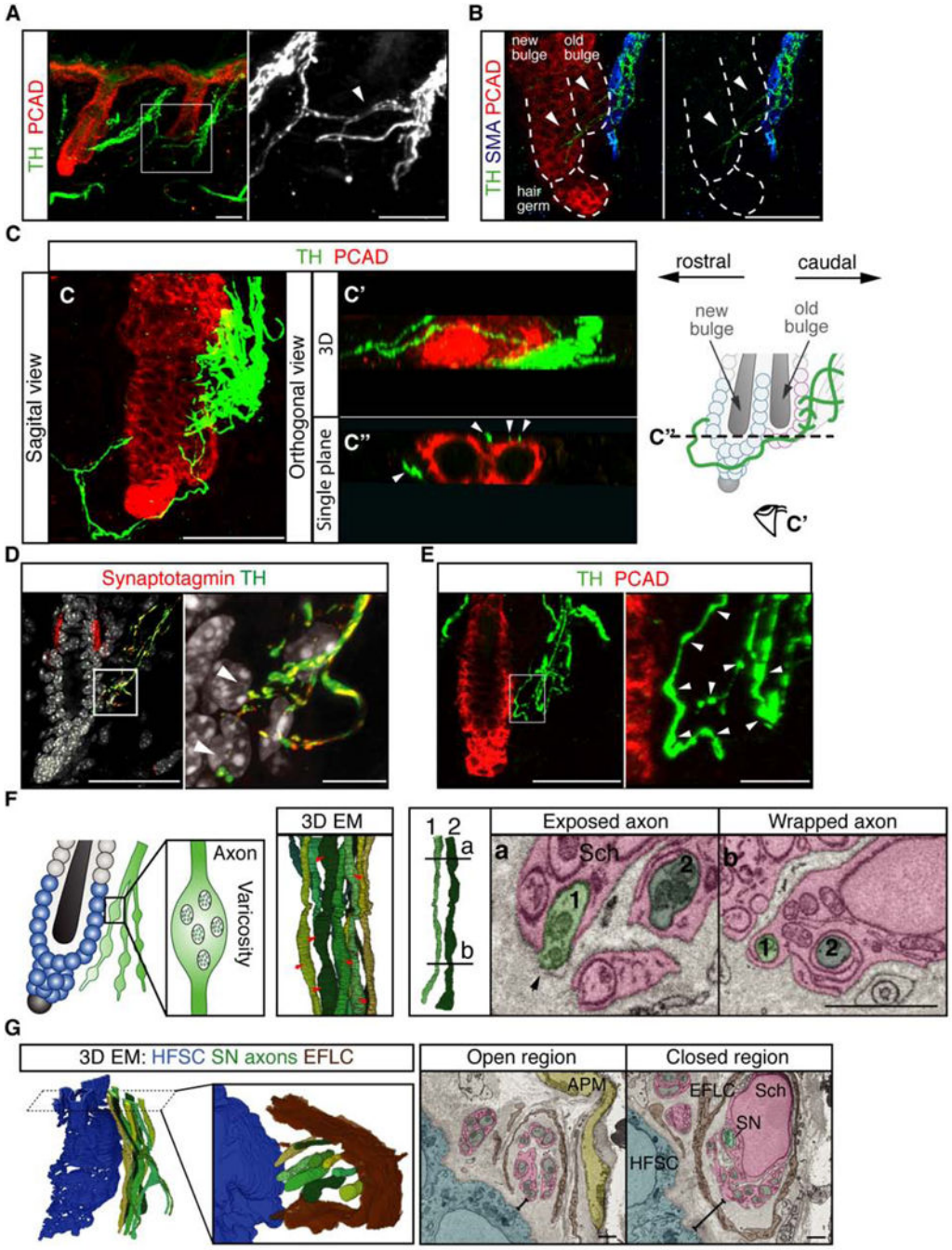

Figure 4. A sympathetic network surrounds HFSCs and forms synapse-like connections with HFSCs.

(**A**) Immunofluorescent staining for TH and PCAD reveals a sympathetic network. Insert: nerve bridges (arrowhead) between the main bundles. (**B**) Immunofluorescent staining for TH, Smooth muscle actin (SMA), and PCAD. Sympathetic nerve fibers (arrowheads) extend beyond APMs and approach HFSCs at both the old and new bulge. (**C**) A main sympathetic bundle innervates the APM and the old bulge (caudal side), while smaller branches from both the caudal and rostral bundles innervate the new bulge and hair germ. (**C'**) Bottom view

of the 3D-reconstructed image in **C**. (**C”**) A single orthogonal section showing points of contact (arrowheads) between HFSCs and sympathetic fibers. Schematic: wrapping of sympathetic nerves (green) around the old bulge (light pink), new bulge (light blue), and hair germ (light blue). Eye cartoon: viewing angle in **C’**. Dashed line: plane of orthogonal view in **C”**. (**D**) Sympathetic nerve fibers colocalize with the pre-synaptic marker Synaptotagmin when approaching HFSCs (arrowheads in insert: points of nerve-HFSC interaction). (**E**) Immunofluorescent staining for TH and PCAD shows varicose axons (arrowheads in insert: varicosities). (**F**) Schematic: synapse-like connections between HFSCs and sympathetic nerves. 3D electron microscope (EM) reconstruction of sympathetic axon terminals demonstrates varicose regions (red arrows). Right: Tracing of the same two axons (axon 1 and axon 2) shows changes in axon diameter and Schwann cell wrapping (Sch, pink). Plane a, varicose region 20 (black arrow: exposed axon). Plane b, non-varicose region. (**G**) 3D-reconstruction of EM stacks showing sympathetic (SN) axons (green), HFSCs (blue), and endoneurial fibroblast-like cells (EFLC, brown, component of endoneurium). Insert shows that endoneurium opens up on the side facing HFSCs to expose enwrapped axons. Right: Single EM sections showing that the endoneurium is closed when sympathetic axons are farther away from HFSCs, but becomes open when the axons approach HFSCs. Scale bar, 10 μm in inserts **D** and **E**; 1 μm in **F** and **G**. See also Figure S4.

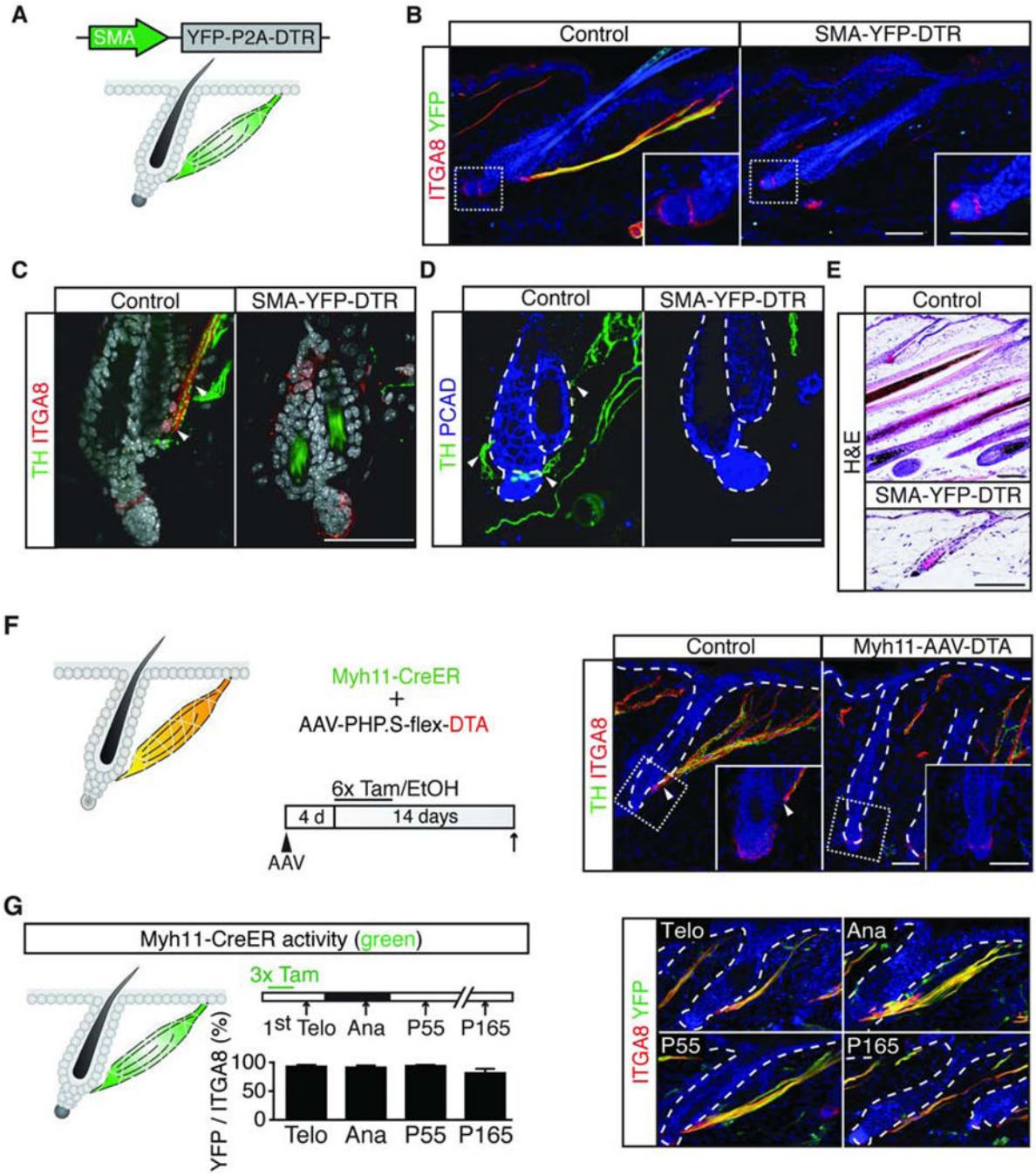

Figure 5. APMs provide stable anchors that maintain sympathetic innervations to HFSCs.

(**A**) Schematic: SMA-YFP-DTR construct and expression patterns (green). (**B**) Co-localization of YFP and ITGA8 in diphtheria toxin (DT) injected control and *SMA-YFP-DTR* mice. (**C, D**) TH and ITGA8 immunofluorescent staining (in **C**) and TH and PCAD immunofluorescent staining (in **D**) in DT injected control and *SMA-YFP-DTR* mice (n = 3 mice per condition). Arrowheads: APMs in **C** and points of nerve-HFSC interaction in **D**. Loss of APMs leads to loss of sympathetic innervations to HFSCs. (**E**) H&E staining in DT injected control and *SMA-YFP-DTR* showing a delay in anagen entry of APM ablated mice

(n = 3 mice per condition). (**F**) Schematic: experimental design. APMs are the only cells that carry both Myh11-CreER and AAV-PHP.Sflex-DTA. Immunofluorescent staining for TH and ITGA8 in *Myh11-CreER* mice injected with AAV-PHP.S-flex-DTA (control: treated with EtOH; Myh11-AAV-DTA: treated with 4-OH-tamoxifen) shows the absence of HFSC innervation in APM ablated mice (n = 4 mice per condition). (**G**) Schematic: Myh11-CreER activity (green) and experimental design (arrows: harvesting). Immunofluorescence and quantification of ITGA8 and YFP colocalization in *Myh11CreER; Rosa-lsl-YFP* mice (n = 3 mice, 7 – 12 APMs per mouse). Tam, tamoxifen or 4-OHtamoxifen; Telo, telogen; Ana, anagen. See also Figure S5.

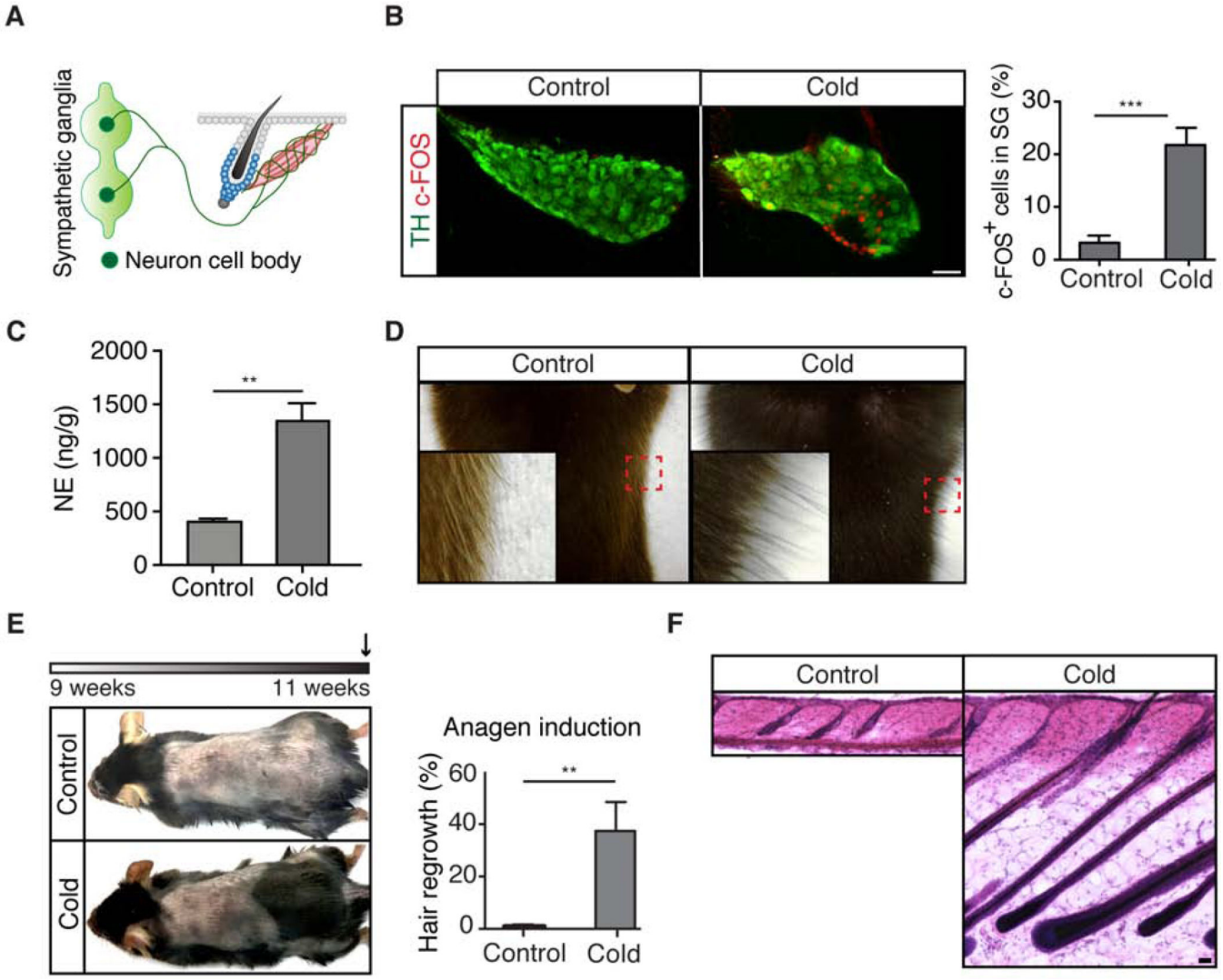

Figure 6: Cold temperature causes piloerection and HFSC activation.

(**A**) Schematic showing sympathetic axons extend to HFSCs while cell bodies are at the sympathetic ganglia. (**B**) Immunofluorescent staining of TH and c-FOS in the sympathetic ganglia from mice under thermoneutral (control) or cold exposure for 2 hours. Graph: % of c-FOS positive cells per ganglion (n = 2 mice per condition, 3 – 5 ganglia per animal). (**C**) Norepinephrine concentration in the skin after 2 hours of cold exposure (n = 6 mice per condition). (**D**) Cold exposure results in piloerection (goosebumps). Magnification of the boxed area shows erection of the hair. (**E**) Schematic: experimental design (arrow: harvesting). 2 weeks of cold exposure in 2nd telogen results in premature anagen entry (n = 9 mice per condition). Graph: % of hair regrowth in back skin. (**F**) H&E staining of control and 2-week cold exposed skin. Data are mean ± SEM. *: p<0.05; **: p<0.01; ***: p <0.001.

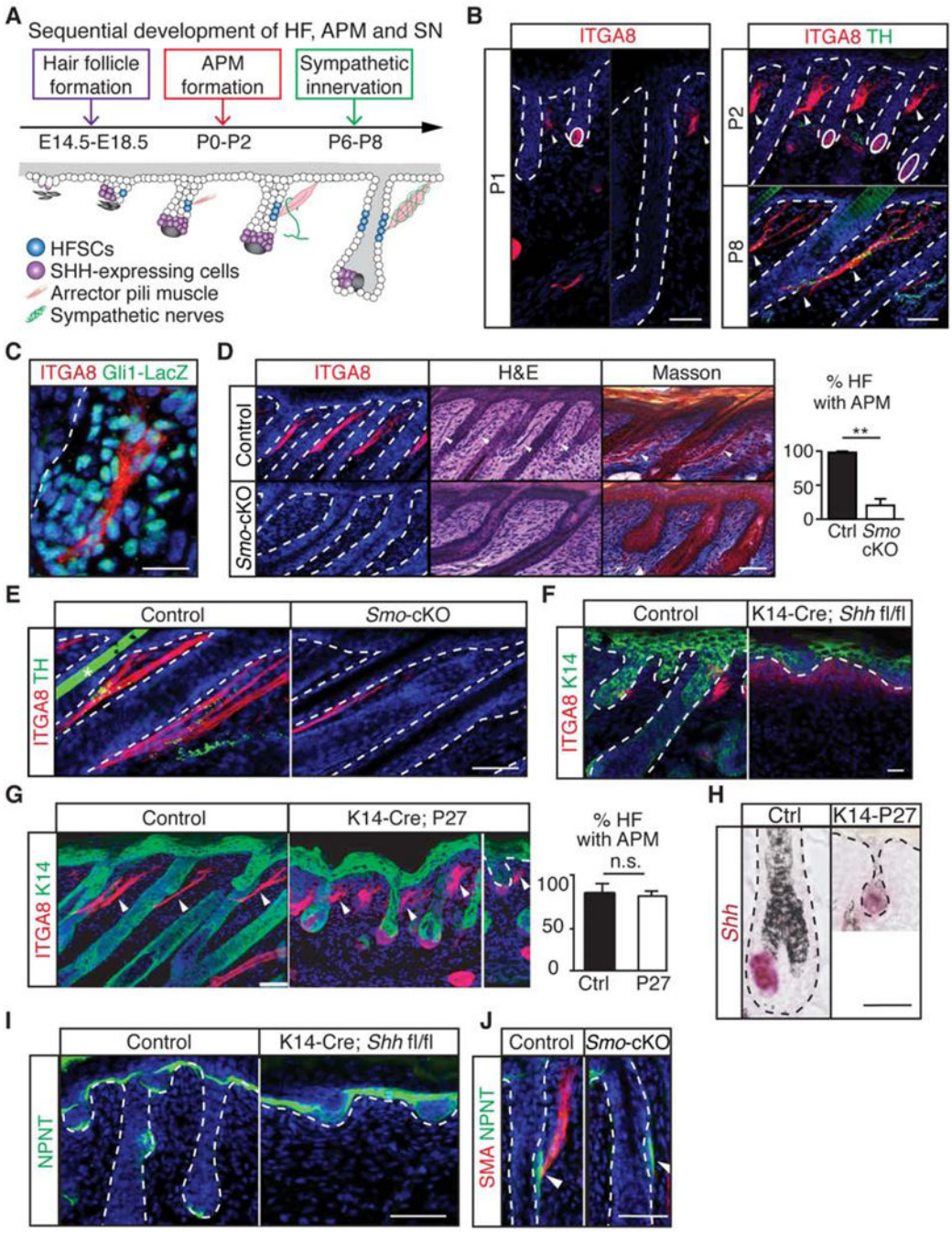

Figure 7. SHH regulates APM development and sympathetic innervation to HFSCs.

(**A**) Schematic: sequential development of hair follicles, APMs, and sympathetic innervations. (**B**) Immunofluorescent staining of ITGA8 and TH. Arrowheads: APMs; solid circles: dermal papilla. (**C**) LacZ and ITGA8 co-localization at P2 Gli1-LacZ skin. (**D**) ITGA8, H&E, and Masson trichrome staining of control and *Pdgfra-Cre; Smo fl/fl* (*Smo*-cKO) mice at P4. Graph: % of HFs with APMs (n = 3 mice per condition, 200 – 280 HF per mouse). (**E**) ITGA8 and TH immunofluorescent staining on control and *Smo*-cKO mice at P8. (**F**) Keratin 14 (K14) and ITGA8 immunofluorescent staining of control and *K14-Cre;*

Shh fl/fl on P0 skin. (**G**) K14 and ITGA8 immunofluorescent staining of control and *K14-Cre; Rosa-lsl-rtTA; TetO-P27* (*K14-P27*) mice on P4 skin. Graph: % of HFs with APMs (n = 2 mice per condition, 120 – 180 HF per mouse). (**H**) *In situ* hybridization of *Shh* in control and *K14-P27* mice at P4. (**I-J**) Immunofluorescent staining of nephronectin (NPNT) in control, *K14-Cre*; *Shh fl/fl* (**I**) and *Smo*cKO (**J**) mice. Data are mean ± SEM. *: $p<0.05$; **: $p<0.01$; ***: $p<0.001$. n.s.: not significant. See also Figure S6 and S7.